Department of Physics and Astronomy

University of Heidelberg

Master thesis

in Physics

submitted by

Zhongyi Feng

born in Beijing (China)

Issued 2014

Observation and Characterization of the Bichromatic Force on Metastable Argon-40

This Master thesis has been carried out by Zhongyi Feng

at the

Kirchhoff Institute for Physics

under the supervision of

Prof. Dr. Markus K. Oberthaler

Observation and Characterization of the Bichromatic Force on Metastable Argon-40

The ^{39}Ar dating accuracy of the Atom Trap Trace Analysis experiment in Heidelberg is depending on the sample size and measuring time which can be reduced by increasing the current atmospheric ^{39}Ar count rate of $[3.58 \pm 0.10]$ $\frac{\text{atoms}}{\text{h}}$. The collimator has great scope for improvements as it can only address $\sim$ 10% of the atoms leaving the source due to its limited capture range. Therefore, faster transverse atoms have to be cooled down beforehand, but due to the short interaction time, a strong light force is necessary to capture them. The bichromatic force is using two frequencies that are equally detuned from atomic resonance to exceed the limits of the radiative force. Its demonstration and characterization on a collimated beam of metastable ^{40}Ar atoms is presented in this work. Basically, the force is only limited by the available power and was determined experimentally and theoretically in dependence of optical power, relative phase, detuning and Doppler shift of the atoms. In the scope of this work, the optics for the required frequencies have been set up and the theoretical values have been calculated with the π-pulse model, Dressed States and optical Bloch equations. A bichromatic force of $[2.95 \pm 0.54]F_{\text{rad}}$ was measured with the experimental accessible parameters which corresponds to $\sim$ 80% of the theoretical predicted value.

Beobachtung und Charakterisierung der Bichromatischen Kraft an Metastabilem Argon-40

Die Genauigkeit der ^{39}Ar Datierung vom Atom Trap Trace Analysis Experiment in Heidelberg hängt von der Probengröße und Messzeit ab, die durch Erhöhung der derzeitigen atmosphärischen Zählrate von $[3.58 \pm 0.10]$ $\frac{\text{Atomen}}{\text{h}}$ reduziert werden können. Der Kollimator bietet viel Raum für Verbesserungen, da er wegen seines limitierten Einfangbereiches nur $\sim$ 10% der Atome adressieren kann, welche die Quelle verlassen. Transversal schnellere Atome müssen deswegen zwischen Quelle und Kollimator verlangsamt werden, wofür aufgrund der kurzen Interaktionszeit eine starke Lichtkraft benötigt wird. Die bichromatische Kraft verwendet zwei Frequenzen, die gleichermaßen von der Atomresonanz verstimmt sind, um das Limit der radiativen Kraft zu überschreiten. Ihre Demonstration und Charakterisierung an einem kollimierten Strahl von metastabilen ^{40}Ar Atomen wird in dieser Arbeit gezeigt. Die Kraft ist prinzipiell nur durch die verfügbare Leistung limitiert und wurde in Abhängigkeit von optischer Leistung, relativer Phase, Verstimmung und Dopplerverschiebung der Atome experimentell und theoretisch bestimmt. Im Rahmen dieser Arbeit wurde hierfür die Optik zur Erzeugung der benötigten Frequenzen aufgebaut und die theoretischen Werte wurden mit Hilfe von π-Puls Modell, Dressed-Atom-Modell und optischen Bloch Gleichungen berechnet. Mit den experimentell zugänglichen Parametern wurde eine bichromatische Kraft von $[2.95 \pm 0.54]F_{\text{rad}}$ gemessen, die $\sim$ 80% des berechneten Wertes entspricht.

Contents

Preface **1**

1 Fundamentals **3**

1.1 Atom Trap Trace Analysis . . . 3

1.2 Properties of Argon-40 . . . 4

1.3 Interaction of Atoms with Light . . . 6

1.3.1 Rabi Oscillations . . . 6

1.3.2 The Dressed Atom Picture . . . 9

1.3.3 Spontaneous Emission . . . 11

1.3.4 Optical Bloch Equations . . . 12

1.3.5 Optical Forces . . . 13

2 The Bichromatic Force **16**

2.1 π-Pulse Model . . . 16

2.2 Doubly Dressed Atom Model . . . 19

2.3 Numerical Calculations . . . 26

2.4 Corrections for Gaussian Laser Beams . . . 30

3 Experimental Setup **38**

3.1 Four-Frequency Generation . . . 38

3.2 Tapered Amplifier for Strong Pulse Trains . . . 41

3.3 Interaction Zone and Detection of the Deflected Atom Beam . . . 43

4 Measurements of the Bichromatic Force **46**

4.1 Atom Beam Imaging . . . 46

4.2 Observation of the Bichromatic Force 47
4.3 Characterization of the Bichromatic Force 49
4.4 Bichromatic Precollimator 56

5 Conclusion **58**
5.1 Summary 58
5.2 Conclusion and Outlook 59

Appendix **63**

Bibliography **66**

Acknowledgement **70**

Preface

The radioactive isotopes of noble gases play important roles in environmental physics and are used for different dating methods, as they are inert due to their electronic configuration [1]. Argon and krypton are part of the atmosphere and two of their radioactive isotopes[1] are of special interest due to the half-lives of 269 years for ^{39}Ar and 229.000 years for ^{81}Kr [2]. However, the low relative atmospheric abundance $\frac{^{39}\mathrm{Ar}}{\mathrm{Ar}} = 8 \cdot 10^{-16}$ and $\frac{^{81}\mathrm{Kr}}{\mathrm{Kr}} = 5 \cdot 10^{-13}$ [3] hinders the routine use of established techniques such as Low-Level Counting (LLC) and Accelerator Mass Spectrometry (AMS) [4] due to sample sizes, measurement times and costs.

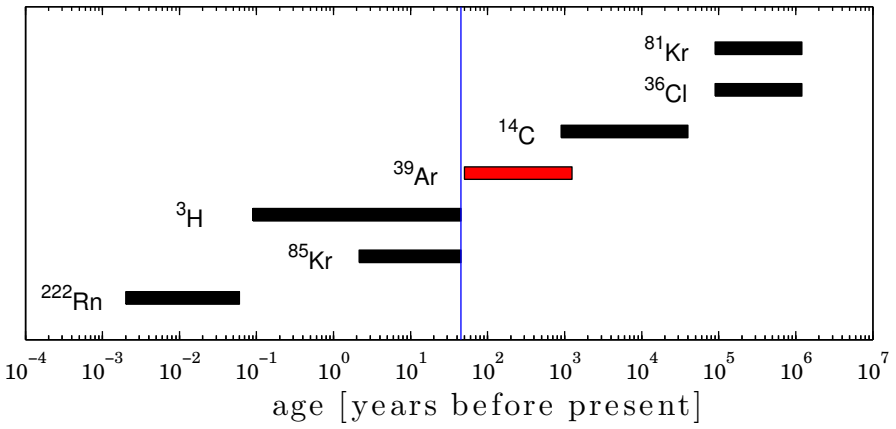

Figure 1: Dating ranges of different radioactive tracers that are important in hydrology (adapted from [5]). Several nuclear bomb tests have been performed in the 1950's which created some fast decaying isotopes and the vertical line marks the bomb peak in 1955 [6]. ^{39}Ar has a half-life of 269 years [2] and covers a range where no other isotopes are available.

[1]Another interesting tracer is the anthropogenically produced ^{85}Kr with half-life of 10.8 years.

Atom Trap Trace Analysis (ATTA) is a method that has been developed in the past two decades for routine measurements of rare ^{81}Kr using standard techniques of atom optics [7]. On an atomic level, the mass difference and nuclear spin shifts the resonance frequency of the transitions of interest in the range of a few hundred MHz. The isotopes become distinguishable if many cycles of absorption and spontaneous emission are considered, which is the case in a Magneto-Optical Trap (MOT) [8]. The ATTA experiment in Heidelberg is a collaboration between the environmental physics group of Prof. Dr. Werner Aeschbach-Hertig and the atom optical group of Prof. Dr. Markus K. Oberthaler and focuses on argon [9]. The half-life of 269 years for ^{39}Ar [2] covers a gap between 50 and 1000 years before present that is not occupied by other isotopes as shown in Figure 1. Thus, ^{39}Ar is suitable for dating of groundwater and alpine glaciers in the time span of anthropogenic influences.

The current count rate of ATTA in Heidelberg is $[3.58 \pm 0.10]\ \frac{\text{atoms}}{\text{h}}$ for atmospheric ^{39}Ar [10]. This has to be improved for increasing the accuracy of measurements or to reduce the sample size and measuring time. A collimator is used for transverse cooling of the metastable argon beam that has a HWHM of $\sim 85\frac{\text{m}}{s}$ when leaving the source [11]. Due to the limited capture range $\sim \pm 30\frac{\text{m}}{s}$ of the collimator [10], only about one tenth of the atoms are actually reaches the MOT. To increase the count rate, faster atoms have to be slowed down between the source and collimator but a strong force is necessary due to the short interaction time.

A possible candidate for this purpose is the bichromatic force that exceeds the radiative force if certain conditions can be fulfilled. It was first proposed in [12] and uses two frequencies detuned equally from atomic resonance. So far, it has been demonstrated for Na [12], Cs [13], Rb [14] and He [15]. In the scope of this work, it is shown for the first time on metastable ^{40}Ar atoms to study the possible applications for the ATTA experiment that have been proposed in [16].

Chapter 1

Fundamentals

1.1 Atom Trap Trace Analysis

The Atom Trap Trace Analysis experiment in Heidelberg is developed to perform routine measurements of ^{39}Ar using standard techniques of atom optics. The ^{39}Ar isotope is of special interest in environmental physics due to its half-life of 269 years and is detected on a single atom counting level in ATTA [17, 18]. The low relative abundance of $\frac{^{39}\mathrm{Ar}}{\mathrm{Ar}} = 8 \cdot 10^{-16}$ [3] requires an efficient apparatus and since the current count rate of ^{39}Ar is only $3.58 \pm 0.10 \frac{\text{atoms}}{\text{h}}$ [10], the stability of the system has to be ensured for a few days.

Figure 1.1 shows a schematic diagram of the most important components[1] of the current ATTA setup. The parts are only briefly described here as they are well documented in past publications of the workgroup [5, 16, 18--21]. A more detailed schematic diagram can be found in Appendix A.

The ground state argon atoms enter the apparatus in the nitrogen cooled source, where a RF-discharge excites a part to the metastable level of interest. A collimator with a tilted mirror design is used for transverse cooling and the atom beam is further focused with a two-dimensional Magneto-Optical Trap that is called Magneto-Optical Lens (MOL) in the setup. The Zeeman-Slower reduces the velocity distribution so that the longitudinal

[1] The exact efficiencies of these components at the time of this work can be found in [16].

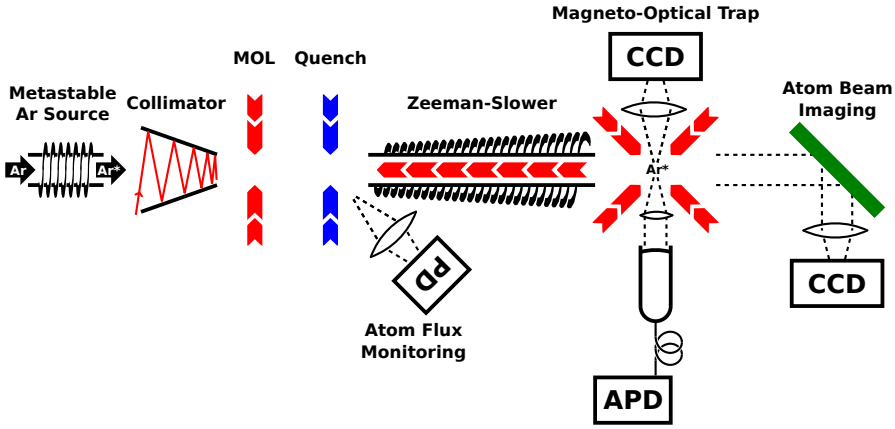

Figure 1.1: The setup of the Atom Trap Trace Analysis experiment in Heidelberg. The compontens are from left to right: metastable argon source, transverse collimator, Magneto-Optical Lens (MOL), ^{40}Ar quench laser beam, Zeeman-Slower, Magneto-Optical Trap (MOT), atom beam imaging tool.

velocity of the atoms are low enough to be caught in the subsequent three-dimensional Magneto-Optical Trap. There, a CCD camera and an Avalanche Photodiode (APD) are used to detect the fluorescence of single trapped atoms.

The design of the laser system enables switching to the resonances of different isotopes, especially the stable references ^{40}Ar and ^{38}Ar and the radioactive ^{39}Ar. The different frequencies needed are documented in [20]. The atom beam imaging tool maps the cross section of an ^{40}Ar beam to a CCD camera and can be used for adjustments of the setup. For detection of ^{39}Ar, a quench transition [21] is used to reduce the ^{40}Ar background by pumping these metastables back to the ground state. The fluorescence signal of the quench is also used as an atom flux monitoring to quantify the efficiency of the source.

1.2 Properties of Argon-40

In this work, only ^{40}Ar is used to observe and measure the bichromatic force as it is much easier to handle due to the relative abundance of 99.9% and its vanishing nuclear spin.

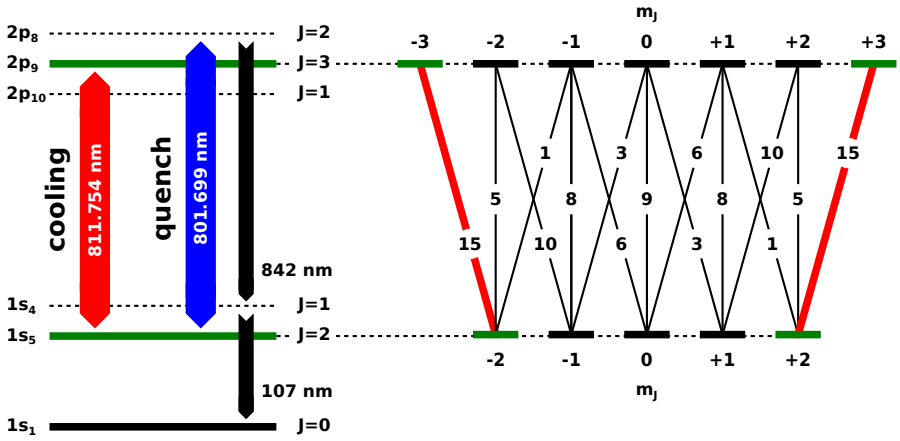

Figure 1.2: A schematic diagram of the ^{40}Ar energy levels that are of interest for this work given in Paschen notation [19]. The cooling transition from the metastable $1s_5$ to $2p_9$ is closed due to the selection rule $\Delta J = 0, \pm 1$ of the total angular momentum. The levels split further into different magnetic sublevels m_J with different transition strengths, where circular polarized light can be used to couple the stretched states. A quenching transition can be used to excite the metastable ^{40}Ar atoms to the $2p_8$ level, from where they decay to the ground state. A more detailed level scheme is given in Appendix B.

Figure 1.2 shows a schematic diagram of the ^{40}Ar energy levels that are of interest in the scope of this work. The states are given in Paschen-Notation [19]. As described in the last section, the ground state argon atoms are excited with a RF-discharge in the nitrogen cooled source tube. This process distributes the atoms into different higher states where two metastable states with forbidden dipole transition to the ground state exist. The relevant state for ATTA is the $1s_5$ metastable level since a closed transition to the $1p_9$ level exists due to the selection rule $\Delta J = 0, \pm 1$ of the total angular momentum. This transition is used for laser cooling in the experiment.

The states of the closed transition $1s_5 \rightarrow 2p_9$ split further into magnetic sublevels with $m_J = -J, -J+1, ..., +J$. This leads to a lot of possible excitations, that are shown in Figure 1.2, where the strength of these transitions is normalized to the weakest dipole moment. The selection rule for the magnetic sublevels is $\Delta m_J = 0$ for linearly polarized light (π) and $\Delta m_J \pm 1$ for circularly polarized light (σ^+ or σ^-). Using one of the latter will drive the ^{40}Ar atom into the stretched states with maximal m_J where it can be regarded as two-level system since only transitions with $m_J = \pm 2 \leftrightarrow m_J = \pm 3$ occur.

Another important transition is from the metastable $1s_5$ to $2p_8$, from where the dipole transition to the $1s_4$ level is allowed. There, the atom will decay further down to the ground state, which can not be addressed by the laser system anymore. This process allows the control of the metastable ^{40}Ar atom flux, as the atoms can be completely quenched out of resonance. In a ^{39}Ar measurement, this reduces the background due to off-resonant excitations of ^{40}Ar in the MOT. The 842 nm fluorescence signal is monitored [16] and can be used to quantify the atom flux since each atom emits only one photon.

1.3 Interaction of Atoms with Light

This section deals with atom-light interactions and gives a brief summary of the basic concepts that have been developed in the past century. It mainly follows [22] and covers those aspects that are necessary for understanding bichromatic cooling.

1.3.1 Rabi Oscillations

The description starts with an atom in an electromagnetic field. The time-dependent Schrödinger equation is:

$$\hat{H}|\Psi(\vec{r},t)\rangle = i\hbar\frac{\partial}{\partial t}|\Psi(\vec{r},t)\rangle \tag{1.1}$$

Here, $\hat{H}$ is the total Hamiltonian of the system, $|\Psi\rangle$ the one electron wavefunction and $\vec{r}$ the coordinate of the electron. A semiclassical approach, where the atom is treated quantum mechanically with a classical radiation field leads to the separation $\hat{H} = \hat{H}_0 + \hat{H}'(t)$. The interaction of the atom with the light field is given by $\hat{H}'(t)$ and the atomic part can be described by the time-independent Schrödinger equation

$$\hat{H}_0|\Phi_n(\vec{r})\rangle = E_n|\Phi_n(\vec{r})\rangle \tag{1.2}$$

where $\hat{H}_0$ is the field-free atomic Hamiltonian with eigenvalues $E_n = \hbar\omega_n$ and corresponding eigenfunctions $|\Phi_n\rangle$. Using the time-evolution operator $\hat{U}(t) = e^{-i\frac{\hat{H}_0}{\hbar}t}$ [23],

the wavefunction $|\Psi(\vec{r},t)\rangle$ can be expanded in the basis $\{|\Phi_n(\vec{r})\rangle\}$:

$$|\Psi(\vec{r},t)\rangle = \sum_k c_k(t)|\Phi_k(\vec{r})\rangle e^{-i\omega_k t} \tag{1.3}$$

The $c_k(t)$'s are the time-dependent coefficients of the orthogonal sum. Using (1.3) and the separated Hamiltonian from above in the time-dependent Schrödinger equation (1.1), the scalar product with $\langle\Phi_j|$ leads to the time-evolution of the coefficients

$$i\hbar\frac{\mathrm{d}c_j}{\mathrm{d}t} = \sum_k c_k(t)H'_{jk}(t)e^{i\omega_{jk}t} \tag{1.4}$$

with $H'_{jk} = \langle\Phi_j|\hat{H}'|\Phi_k\rangle$ and $\omega_{jk} = \omega_j - \omega_k$. Unfortunately, this general result is unsolvable and approximations have to be employed. The usual approach is to consider a two-level system, where only two terms of the summation in (1.4) are left. By absorbing all diagonal terms of $\hat{H}'(t)$ into $\hat{H}_0$, the time-evolution of the coefficients becomes:

$$i\hbar\dot{c_g} = c_e(t)H'_{ge}(t)e^{-i\omega_A t} \tag{1.5a}$$

$$i\hbar\dot{c_e} = c_g(t)H'_{eg}(t)e^{i\omega_A t} \tag{1.5b}$$

The indices g and e are for ground and excited state respectively and the resonance frequency is $\omega_A = \omega_{eg}$. The expected classical dipole operator [22]

$$\hat{H}'(t) = -e\vec{\mathcal{E}}(\vec{r},t)\cdot\vec{r} \tag{1.6}$$

can be evaluated with a plane wave in z-direction: $\vec{\mathcal{E}}(\vec{r},t) = E_0\vec{\epsilon}\cos(\omega_L t - kz)$. Since the wavelength $\lambda_l = \frac{2\pi c}{\omega_L}$ of the light field is several orders of magnitude larger than the region containing the wavefunctions $|\Phi_n(\vec{r})\rangle$, the electric field $\vec{\mathcal{E}}(\vec{r},t)$ can be considered as constant over the extent of an atom. This is the so-called electric dipole approximation [24]. Using the Rabi frequency

$$\Omega := \frac{-eE_0\vec{\epsilon}}{\hbar}\langle e|\vec{r}|g\rangle \tag{1.7}$$

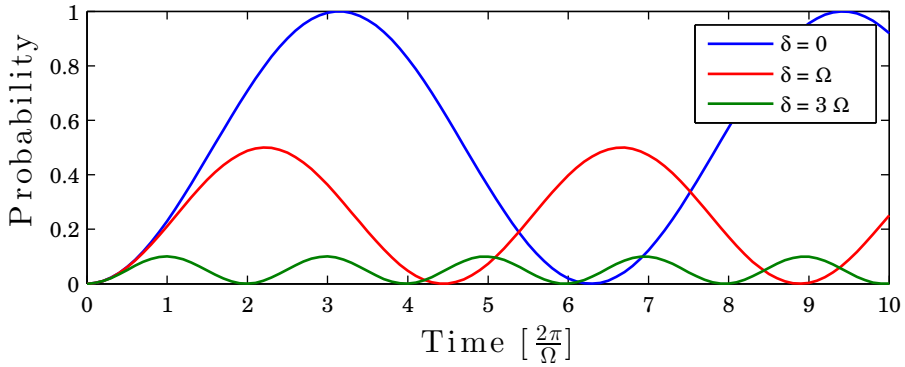

Figure 1.3: Rabi oscillations of $|c_e|^2$ with frequency $\Omega' = \sqrt{\Omega^2 + \delta^2}$ give the probability for an atom to be in the excited state. The amplitude decreases for larger detunings whereas the frequency of the oscillations is increasing.

the off-diagonal elements of the interaction Hamiltonian become $H'_{eg}(t) = \hbar\Omega \cos(\omega_L t - kz)$. Inserting this into (1.5) with $H'_{ge}(t) = H'_{eg}(t)^*$ and $z = 0$ gives:

$$i\hbar\dot{c_g} = c_e\hbar\Omega^* \cos(\omega_L t)e^{-i\omega_A t} = \frac{\hbar\Omega^*}{2}c_e(e^{i(\omega_L-\omega_A)t} + e^{-i(\omega_L+\omega_A)t}) \tag{1.8a}$$

$$i\hbar\dot{c_e} = c_g\hbar\Omega \cos(\omega_L t)e^{i\omega_A t} = \frac{\hbar\Omega}{2}c_g(e^{i(\omega_L+\omega_A)t} + e^{-i(\omega_L-\omega_A)t}) \tag{1.8b}$$

The time-evolution contains slow oscillating terms with frequency $\delta := \omega_L - \omega_A$ and fast oscillating terms with $\omega_L + \omega_A$. The rotating wave approximation can be used here by neglecting the fast oscillating terms. Then the result reduces to:

$$i\hbar\dot{c_g} = \frac{\hbar\Omega^*}{2}c_e e^{i\delta t} \tag{1.9a}$$

$$i\hbar\dot{c_e} = \frac{\hbar\Omega}{2}c_g e^{-i\delta t} \tag{1.9b}$$

The second time derivatives of (1.9) can be inserted into each other. Integration of the result leads to:

$$c_e(t) = -i\frac{\Omega}{\Omega'}\sin(\frac{\Omega'}{2}t)e^{-i\frac{\delta}{2}t} \tag{1.10}$$

The effective Rabi frequency is given by $\Omega' = \sqrt{\Omega^2 + \delta^2}$. Figure 1.3 shows the probability $|c_e(t)|^2$ to be in the excited state. The atom undergoes Rabi oscillations at frequency Ω' between excited and ground states.

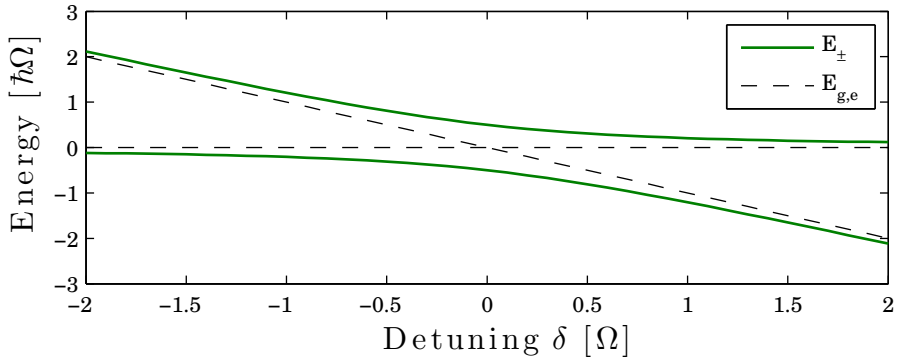

Figure 1.4: The shifted energy levels due to atom-light interaction are given by the solid lines and the bare energy levels of an atom plus light field are given by the dashed lines. The interaction leads to an avoided crossing of the mixed states at $\delta = 0$ with energy separation of $\Delta E = \hbar\Omega$. Large detunings $|\delta| \gg |\Omega|$ shift the energy from the bare states by $\pm\frac{\hbar\Omega^2}{4\delta}$.

The atom-light interaction further shifts the energy of the system away from the energy levels $\{E_n\}$ of the bare atom. The new time-independent eigenvalues of the total Hamiltonian can be found by first transforming into a rotating frame with $c'_g(t) := c_g(t)$ and $c'_e(t) := c_e(t)e^{-i\delta t}$. Inserting this into (1.9) gives the interaction Hamiltonian and its eigenvalues in this frame:

$$\hat{H}' = \frac{\hbar}{2}\begin{pmatrix} 0 & \Omega \\ \Omega^* & -2\delta \end{pmatrix} \qquad \text{with} \qquad E_\pm = \frac{\hbar}{2}(-\delta \mp \Omega') \tag{1.11}$$

In presence of an electromagnetic field, the bare eigenstates $|e\rangle$ and $|g\rangle$ are no longer the eigenvectors of the system. Figure 1.4 shows the detuning dependent energy shifts of the coupled system from the bare energy levels. For large detuning $|\delta| \gg \Omega$, the levels are shifted by $\pm\frac{\hbar\Omega^2}{4\delta}$ and at $\delta = 0$ is an avoided crossing of the energy levels with separation $\Delta E = \hbar|\Omega|$. The new eigenstates are mixtures of ground and excited states and are described in the next section with the dressed atom picture.

1.3.2 The Dressed Atom Picture

The Jaynes-Cummings model or Dressed Atom Picture is a different treatment of the two-level system in which all parts are described quantum mechanically. The total

Hamiltonian includes a quantum mechanical interaction term and a quantized light field [25]:

$$\hat{H}_{JC} = \hat{H}_0 + \hat{H}_{rad} + \hat{H}_{int} = \hbar\omega_A|e\rangle\langle e| + \hbar\omega_L\hat{a}^\dagger\hat{a} + \frac{\hbar\tilde{\Omega}}{2}(\hat{a}^\dagger|g\rangle\langle e| + \hat{a}|e\rangle\langle g|) \quad (1.12)$$

Here, $\tilde{\Omega}$ is the vacuum Rabi frequency describing the coupling strength, $\hat{a}^\dagger$ and $\hat{a}$ are the bosonic creation and annihilation operators defined by

$$\hat{a}^\dagger|n\rangle = \sqrt{n+1}|n+1\rangle \qquad \text{and} \qquad \hat{a}|n\rangle = \sqrt{n}|n-1\rangle \quad (1.13)$$

where $|n\rangle$ is the state of the quantized laser field with n photons. Using the product states $|g,n\rangle$ and $|e,n-1\rangle$ as basis, the Jaynes-Cummings Hamiltonian for $n+1$ photons becomes:

$$\hat{H}_{JC} = \hbar\begin{pmatrix} n\omega_L & \frac{\tilde{\Omega}}{2}\sqrt{n} \\ \frac{\tilde{\Omega}}{2}\sqrt{n} & (n-1)\omega_L+\omega_A \end{pmatrix} = n\hbar\omega_L \cdot \mathbb{1}_2 + \frac{\hbar}{2}\begin{pmatrix} 0 & \Omega_n \\ \Omega_n & -2\delta \end{pmatrix} \quad (1.14)$$

With the n-photon Rabi frequency $\Omega_n = \tilde{\Omega}\sqrt{n}$, the second term in (1.14) resembles the classical interaction Hamiltonian of (1.11). The eigenenergies are

$$E_{\pm,n} = n\hbar\omega_L \pm \frac{1}{2}\hbar\Omega'_n \quad (1.15)$$

where $\Omega'_n = \sqrt{\delta^2 + \Omega_n^2}$. This gives a ladder of eigenenergies separated by $\hbar\omega_L$. The eigenstates are called Dressed States and are linear combinations of the bare ground and the excited state. For the special case of $\delta = 0$, they are:

$$|+\rangle_n = \frac{1}{\sqrt{2}}(|g,n\rangle + |e,n-1\rangle) \qquad \text{and} \qquad |-\rangle_n = \frac{1}{\sqrt{2}}(|g,n\rangle - |e,n-1\rangle) \quad (1.16)$$

Figure 1.5 shows a part of the infinite ladder of eigenstates. For the resonant case $\delta = 0$ and no interaction, the energies of $|g,n+1\rangle$ and $|e,n\rangle$ are degenerated, but coupling to the light field leads to energy separation of $\Delta E = \hbar\Omega'_n$ as in the semi-classical approach.

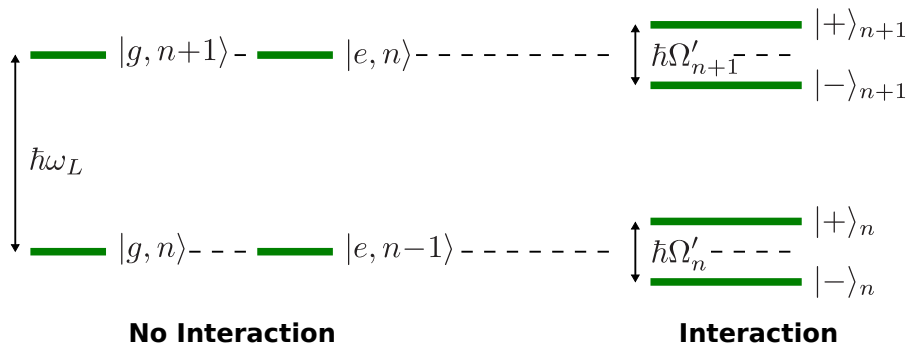

Figure 1.5: The Dressed States $|+\rangle_n$ and $|-\rangle_n$ are the eigenstates of an interacting atom-light system with n photons. The eigenenergies are shifted by $\Delta E = \pm\frac{1}{2}\hbar\Omega'_n$ from the ladder of bare state energy levels that are separated by $\hbar\omega_L$.

1.3.3 Spontaneous Emission

The description so far has not included effects of spontaneous emissions which can be explained by the coupling of the atom to the infinite empty vacuum modes of the electromagnetic field. Using the formalism of Section 1.3.1, the general state of the system is then [22]:

$$|\Psi(t)\rangle = c_e(t)e^{-i\omega_e t}|e, 0\rangle + \sum_S c_{g,1_S}e^{-i(\omega_g+\omega_S)t}|g, 1_S\rangle \tag{1.17}$$

Here, $|e, 0\rangle$ is the excited state and $|g, 1_S\rangle$ are the ground states with one photon in the field and $S = (\vec{k}, \vec{\epsilon})$ denotes the vacuum mode. The vacuum Rabi frequencies $\Omega_S = -\frac{eE_S}{\hbar}\langle e, 0|r|g, 1_S\rangle$ describe the coupling of these modes to the excited state. Using (1.17) in the Schrödinger equation (1.1) leads to the time evolution:

$$i\hbar\dot{c}_e(t) = \sum_S c_{g,1_S}(t)\hbar\Omega_S e^{-i(\omega_S-\omega_A)t} \tag{1.18a}$$

$$i\hbar\dot{c}_{g,1_S}(t) = c_e(t)\hbar\Omega_S^* e^{i(\omega_S-\omega_A)t} \tag{1.18b}$$

The excited state is coupled to all vacuum modes but since the ground state is only coupled to a single state, spontaneous absorption is not possible [22]. The sum in (1.18) can be replaced by an integration over all modes by using the electric field $E_S = \sqrt{\frac{\hbar\omega_S}{2\epsilon_0 V}}$

which can be derived from the zero-point energy of a given volume V and the mode density $\mathrm{d}n = 2 \cdot \frac{V\omega^2}{8\pi^3 c^3} \sin(\Theta)\mathrm{d}\omega\mathrm{d}\Theta\mathrm{d}\Phi$. The time integration of the ground state coefficient (1.18) with these modes gives:

$$\dot{c_e}(t) = -\frac{\gamma}{2}c_e(t) \qquad \text{with} \qquad \gamma = \frac{\omega|\langle e,0|r|g,1_S\rangle|^2}{3\pi\epsilon_0\hbar c^3} \tag{1.19}$$

Spontaneous emission can therefore be described by a single parameter, the spontaneous decay rate γ which is related by $\gamma = \frac{1}{\tau}$ to the lifetime τ of the excited state.

1.3.4 Optical Bloch Equations

The dynamics of the system in presence of spontaneous emission can be described with the density matrix ρ whose components are defined by $\rho_{jk} = \langle\Phi_j|\hat{\rho}|\Phi_k\rangle$, using the density operator $\hat{\rho} = |\Psi\rangle\langle\Psi|$. This leads to:

$$\rho = \begin{pmatrix} \rho_{gg} & \rho_{ge} \\ \rho_{eg} & \rho_{ee} \end{pmatrix} = \begin{pmatrix} c_g c_g^* & c_g c_e^* \\ c_e c_g^* & c_e c_e^* \end{pmatrix} \tag{1.20}$$

The time-evolution of the density matrix is given by the Von-Neumann equation:

$$i\hbar\dot{\rho} = [\hat{H}, \rho] \tag{1.21}$$

Using the interaction Hamiltonian of (1.11) and including spontaneous emission by (1.19) gives the optical Bloch equations (OBE) [22]:

$$\dot{\rho}_{gg} = +\gamma\rho_{ee} + \frac{i}{2}(\Omega^*\rho_{eg} - \Omega\rho_{ge}) \tag{1.22a}$$

$$\dot{\rho}_{ee} = -\gamma\rho_{ee} + \frac{i}{2}(\Omega\rho_{ge} - \Omega^*\rho_{eg}) \tag{1.22b}$$

$$\dot{\rho}_{ge} = -(\frac{\gamma}{2} + i\delta)\rho_{ge} + \frac{i}{2}\Omega^*(\rho_{ee} - \rho_{gg}) \tag{1.22c}$$

$$\dot{\rho}_{eg} = -(\frac{\gamma}{2} - i\delta)\rho_{eg} + \frac{i}{2}\Omega(\rho_{gg} - \rho_{ee}) \tag{1.22d}$$

Figure 1.6 shows the numerical integration of $\dot{\rho}_{ee}(t)$ which gives a damped Rabi oscillation of the excited state probability due to spontaneous emissions. The stationary case

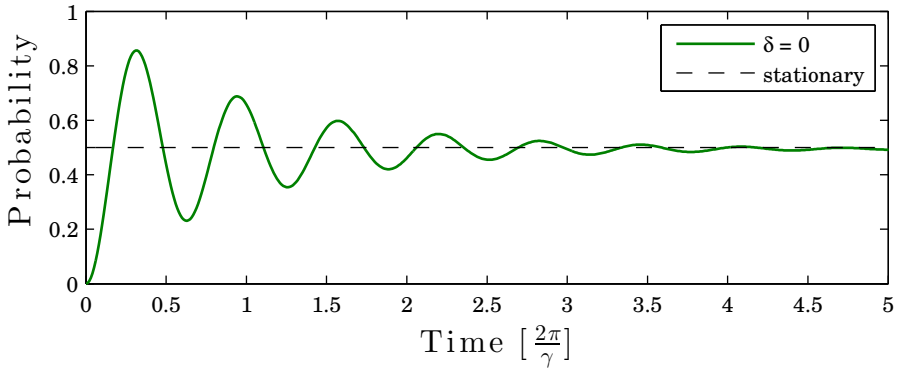

Figure 1.6: The on-resonance probability ρ_{ee} with $\Omega = 10\gamma$ is calculated by numerical integration of the optical Bloch equations and is given by the solid line. Spontaneous emission leads to damping of the Rabi oscillation and the stationary case gives $\rho_{ee} = \frac{1}{2}\frac{s_0}{1+s_0} \approx \frac{1}{2}$ for $\delta = 0$ and high saturation $s_0 \gg 1$ which is represented by the dashed line.

with $\dot{\rho}_{ee} = \dot{\rho}_{eg} = 0$ can be solved analytically and gives the probabilities

$$\rho_{eg} = \frac{i\Omega}{2(\frac{\gamma}{2} - i\delta)(1+s)} \qquad \text{and} \qquad \rho_{ee} = \frac{s_0}{2(1+s_0+(\frac{2\delta}{\gamma})^2)} \tag{1.23}$$

where $s = \frac{s_0}{1+(\frac{2\delta}{\gamma})^2}$ is the saturation parameter and $s_0 = \frac{2|\Omega|^2}{\gamma^2} = \frac{I}{I_S}$ its on-resonance value with the saturation intensity $I_S = \frac{\pi hc}{3\lambda^3\tau}$.

1.3.5 Optical Forces

The interaction of an atom with photons in a light field leads to forces due to momentum exchange in absorption and emission processes. Using Ehrenfest's theorem, the expectation value of the quantum mechanical force operator can be described by the interaction Hamiltonian:

$$\langle \hat{F} \rangle = \frac{\mathrm{d}}{\mathrm{d}t}\langle \hat{p} \rangle = \frac{i}{\hbar}\langle [\hat{H}', \hat{p}] \rangle = -\langle \frac{\partial \hat{H}'}{\partial x} \rangle \tag{1.24}$$

As before, only the off-diagonal elements $\hat{H}'_{ge} = \hat{H}'^{*}_{eg}$ are left in the Hamiltonian of (1.6). With $\langle \frac{\partial \hat{H}'}{\partial x} \rangle = \mathrm{Tr}(\rho \frac{\partial \hat{H}'}{\partial x})$, the Rabi frequency defined in (1.7) and the density matrix in

(1.20), the force F on an atom can be expressed by:

$$\langle \hat{F} \rangle = \hbar(\frac{\partial \Omega}{\partial z}\rho_{eg}^* + \frac{\partial \Omega^*}{\partial z}\rho_{eg}) \tag{1.25}$$

A general Rabi frequency of $\Omega(z) = \omega_R e^{i\phi(z)}$ with magnitude ω_R and a position dependent phase $\phi(z)$ can be used to evaluate (1.25):

$$\begin{aligned} \langle \hat{F} \rangle &= \frac{\hbar}{2}[\frac{\partial \omega_R}{\partial z}(e^{i\phi}\rho_{eg}^* + e^{-i\phi}\rho_{eg}) + i\frac{\partial \phi}{\partial z}(\omega_R e^{i\phi}\rho_{eg}^* - \omega_R e^{-i\phi}\rho_{eg})] \\ &= \hbar\frac{\partial \omega_R}{\partial z}\mathrm{Re}(e^{i\phi}\rho_{eg}^*) + \hbar\frac{\partial \phi}{\partial z}\mathrm{Im}(\omega_R e^{i\phi}\rho_{eg}^*) \end{aligned} \tag{1.26}$$

The two terms in (1.26) can be associated with different types of force which occur for specific choices of the light field. For the case of a travelling wave with the wave vector k, the intensity is constant but the phase is changing spatially, so that $\frac{\partial \omega_R}{\partial z} = 0$ and $\frac{\partial \phi}{\partial z} = k$. Using the stationary solution of the OBE in (1.23) gives the radiative force [22]:

$$F_{rad} = \hbar k \mathrm{Im}(\omega_R e^{i\phi}\rho_{eg}^*) = \frac{\hbar k |\Omega|^2 \gamma}{4(\frac{\gamma^2}{4} + \delta^2)(1+s)} = \hbar k \gamma \rho_{ee} \tag{1.27}$$

This result can be interpreted as the momentum transfer $\hbar k$ at scattering rate $\gamma_P = \gamma\rho_{ee}$. Since the on-resonance probability $\rho_{ee} = \frac{s_0}{2(1+s_0)}$ saturates for high intensities, the radiative force is limited by:

$$F_{rad,max} = \frac{\hbar k \gamma}{2} \tag{1.28}$$

A completely different result can be derived with two counter-propagating waves each with wave number k which form a standing wave. Here, the phase is constant but the intensity is changing, so that $\frac{\partial \phi}{\partial z} = 0$ and $\frac{\partial \omega_R}{\partial z} = -\omega_R k \tan(kz)$. This gives the dipole force [22]:

$$F_{dip} = \hbar\frac{\partial \omega_R}{\partial z}\mathrm{Re}(e^{i\phi}\rho_{eg}^*) = \frac{2\hbar k \delta s_0 \sin(2kz)}{1 + 4s_0\cos^2(kz) + (\frac{2\delta}{\gamma})^2} \tag{1.29}$$

In comparison to the radiative force, this is not limited and can be made arbitrary large at certain positions. However, due to sign reversals on the wavelength scale, the spatial average of the dipole force vanishes for the simple case of a two-level system.

A non-vanishing average force can be achieved by considering multi-level atoms such as in Sisyphus cooling or using light fields with more than one frequency. The bichromatic force can be seen as a special case of non-vanishing dipole force, where two equal detuned frequencies are used for rectification.

Chapter 2

The Bichromatic Force

The bichromatic force arises in counter-propagating beams consisting of two frequencies each detuned by $\pm\Delta$ from the atomic resonance ω_A. As mentioned in the previous chapter, it can be considered as a rectification of the dipole force to create a non-vanishing average force which is, unlike the radiative force, not fundamentally limited by (1.28) and can be made much larger if certain conditions are fulfilled [26].

2.1 π-Pulse Model

The π-pulse model gives a very intuitive but not accurate description of the bichromatic force which is often used in previous works [13--15, 22, 27] as a starting point to understand the basic principles.

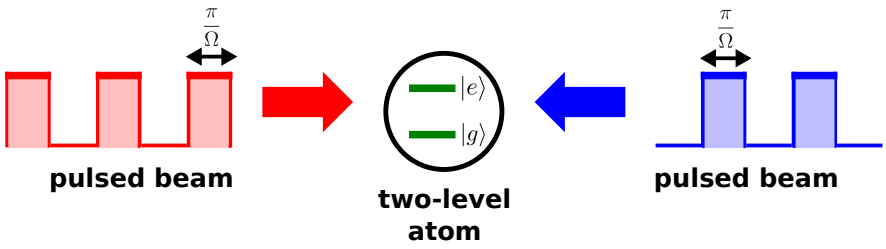

Figure 2.1: In the π-pulse model, the beams are described by discrete intensity pulses with duration $\Delta t = \frac{\pi}{\Omega}$. Each pulse drives half of a Rabi period and changes the state of the atom from ground to excited and vice versa. Coherent sequences of absorption from one side and stimulated emission from the other side exert a force on the atom, which exceeds the radiative limit, if $\Omega \gg \gamma$.

A pair of counter-propagating beams is considered as sequence of discrete intensity pulses as shown in Figure 2.1. The light frequency is on atomic resonance ω_A and the pulse duration is $\Delta t = \frac{\pi}{\Omega}$, where Ω is the Rabi frequency. In this configuration, each pulse will drive the atom by half a Rabi period changing the state from ground to excited and vice versa. If the relative phase difference of the beams is $\Delta\phi = \pi$, the pulses arrive alternately from both sides. Absorption from one direction followed by stimulated emission to the other direction acts as a force on the atom which transfers twice the recoil momentum $\Delta p = 2\hbar k$ per cycle.

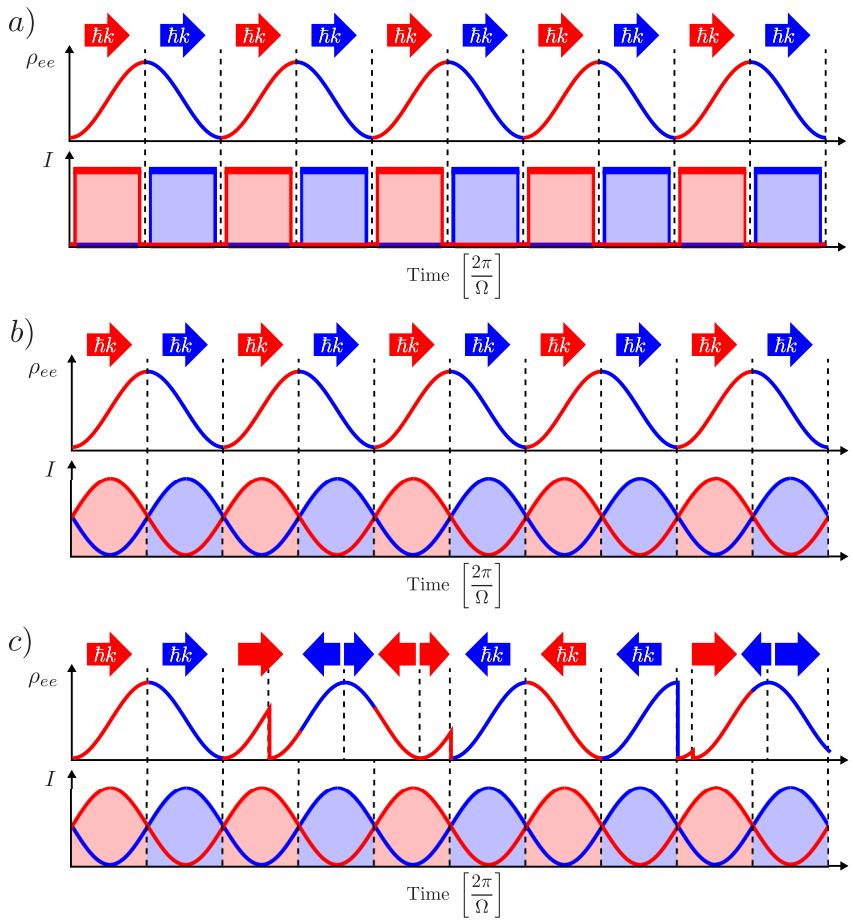

Figure 2.2: (a) The discrete π-pulses are driving the Rabi oscillation alternately from both directions. A momentum of $\Delta p = 2\hbar k$ is coherently transferred per cycle. (b) The beating of two frequencies is used instead of π-pulses. The same momentum transfer rate can be achieved, if beat overlaps are neglected. (c) Spontaneous emissions destroy the coherence, the force even changes signs so that the average vanishes.

This prodecure of coherent momentum transfer is shown in Figure 2.2a. It can exceed

the limit of the radiative force if $\frac{1}{\Delta t} \gg \gamma$, where γ is the spontaneous decay rate of the excited state, usually in the range of several MHz.

In the scope this work the beating of two frequencies $\omega_A \pm \Delta$ is used as a sinusoidally modulated beam to take the role of the pulse trains, which are difficult to create otherwise. Using this configuration, the total electric field in each beam is [27]:

$$\begin{aligned} E_{tot}(z,t) &= E_{+\Delta}(z,t) + E_{-\Delta}(z,t) \\ &= E_0 \cos\left[(k + \frac{\Delta}{c})z - (\omega_A + \Delta)t\right] \\ &+ E_0 \cos\left[(k - \frac{\Delta}{c})z - (\omega_A - \Delta)t\right] \\ &= 2E_0 \cos(kz - \omega_A t)\cos(\Delta \cdot t - \frac{\Delta}{c}z) \end{aligned} \tag{2.1}$$

Here, E_0 is the amplitude of each single electric field and $k = \frac{2\pi}{\lambda} = \frac{\omega_A}{c}$ is the wave vector. This describes a travelling wave at carrier frequency ω_A with amplitude modulation at beat frequency Δ.

Figure 2.2b shows the alternating intensity beats with $\Delta\phi = \pi$. In this case, the duration of the beats is $\Delta t = \frac{\pi}{\Delta}$. Using the definition of the Rabi frequency (1.7), where $\Omega \propto E_0$, the π-pulse condition is [28]:

$$\int_{-\frac{\pi}{2\Delta}}^{+\frac{\pi}{2\Delta}} 2\Omega \cos(\Delta \cdot t)dt = \pi \qquad \rightarrow \qquad \Omega_\pi = \frac{\pi}{4}\Delta \tag{2.2}$$

Since the Rabi frequency Ω is connected to the intensity by the saturation parameter s_0 in (1.23), it can be chosen to fulfill the π-pulse condition (2.2) for a given detuning Δ.

The bichromatic force can be calculated by the momentum transfer per time, if overlapping of counter-propagating beats are neglected. For $\Delta \gg \gamma$, it exceeds the radiative force for certain choices of the relative phase difference:

$$F_{BC,ideal} = \frac{\Delta p}{\Delta t} = \frac{2\hbar k\Delta}{\pi} \gg \frac{\hbar k\gamma}{2} = F_{rad,max} \tag{2.3}$$

The description so far has not included spontaneous emission, which occurs due to the finite lifetime of the excited state. As shown in Figure 2.2c, random spontaneous emission events destroy the coherence of the system and the force will eventually change direction on the time scale of the decay rate γ. The average force vanishes for antisymmetric beat arrivals from both sides with relative phase difference $\Delta\phi = \pi$.

An asymmetric choice of the relative phase difference can achieve a non-vanishing force, but will increase the overlap of the counter-propagating beams. In the scope of the π-pulse model, asymmetric pulses give the atom less time in the excited state and even if a spontaneous emission occurs, there is more time to correct the direction of momentum transfer. The optimum phase difference for high asymmetry and short beat overlap is $\Delta\phi = \frac{\pi}{2}$, which is derived in the next chapter with the Doubly Dressed Atom model. With this choice, the atom is three times longer in the right cycle [27]. The force is therefore half of the ideal force in (2.3):

$$F_{BC} = \frac{F_{BC,ideal}}{2} = \frac{\hbar k \Delta}{\pi} \tag{2.4}$$

The π-pulse model provides good insight and even some numbers on the bichromatic force, but neglects simultaneous pulses from both directions. Since it considers each beam independently, the π-pulse condition in (2.2) can not be accurate. For better calculations, the Doubly Dressed State model is presented in the next section.

2.2 Doubly Dressed Atom Model

The description of the bichromatic force using dressed states was first proposed in [29] and includes the light field and interaction terms in the total Hamiltonian to get the time-independent eigenenergies of the system. In contrast to the π-pulse model, the same two counter-propagating frequencies $\omega_A \pm \Delta$ are paired together to a blue and a red detuned standing wave. The bare atom state is $|g\rangle$ or $|e\rangle$ and the light field with b blue photons and r red photons is denoted by $|b, r\rangle$. Without coupling, the undressed product states are [30]:

$$
\begin{aligned}
|g,b,r\rangle = |g\rangle \otimes |b,r\rangle \quad \text{with} \quad E_{g,b,r} &= b \cdot \hbar(\omega_A + \Delta) + r \cdot \hbar(\omega_A - \Delta) \\
&= (b+r) \cdot \hbar\omega_A + (b-r) \cdot \hbar\Delta \\
&\text{and} \\
|e,b,r\rangle = |e\rangle \otimes |b,r\rangle \quad \text{with} \quad E_{e,b,r} &= \hbar\omega_A + b \cdot \hbar(\omega_A + \Delta) + r \cdot \hbar(\omega_A - \Delta) \\
&= (b+r+1) \cdot \hbar\omega_A + (b-r) \cdot \hbar\Delta
\end{aligned}
\tag{2.5}
$$

The product state energies are separated by $E_{e,b,r} - E_{g,b,r} = \hbar\omega_A$ and each of them is an infinite manifold of states separated by $\Delta E_{g,b,r} = 2\hbar\Delta$ as shown in Figure 2.3. Since the excited energy levels with $b + r = N$ photons are between the ground energy levels with $b + r = N + 1$ photons, the distance of two uncoupled energy levels is $\Delta E = \hbar\Delta$.

In this model, the bichromatic light field can be coherently redistributed by the atom. For absorption of a red detuned photon with $E_r = \hbar(\omega_A - \Delta)$ and stimulated emission of a blue detuned photon $E_b = \hbar(\omega_A + \Delta)$, the light field gains an energy of $E_b - E_r = 2\hbar\Delta = 2\Delta E$ and the atom loses this amount of kinetic energy, resulting in a force. Changing the role of red and blue detuned photons will reverse the sign of the force, since the atom will gain energy in this case.

The Hamiltonian $\hat{H}_{NC}$ of the uncoupled system is simply the sum of the atomic Hamiltonian $\hat{H}_0 = \hbar\omega_A|e\rangle\langle e|$ in (1.12) and the Hamiltonians of both light fields with different frequencies $\hat{H}_{rad} = \hat{H}_b + \hat{H}_r = \hbar(\omega_A + \Delta)\hat{a}_b^\dagger\hat{a}_b + \hbar(\omega_A - \Delta)\hat{a}_r^\dagger\hat{a}_r$. In analogy to (1.13), $\hat{a}_i^\dagger$ and $\hat{a}_i$ are the photon creation and annihilation operators acting on $|b,r\rangle$ and the index $i = b, r$ denotes the detuning of the photon.

The interaction term can be added similarly to the Jaynes-Cummings model in (1.12) by introducing coupling parameters Ω_b to the blue and Ω_r to the red standing wave. Like the energy levels, it is infinite due to different total photon numbers. Truncation to the

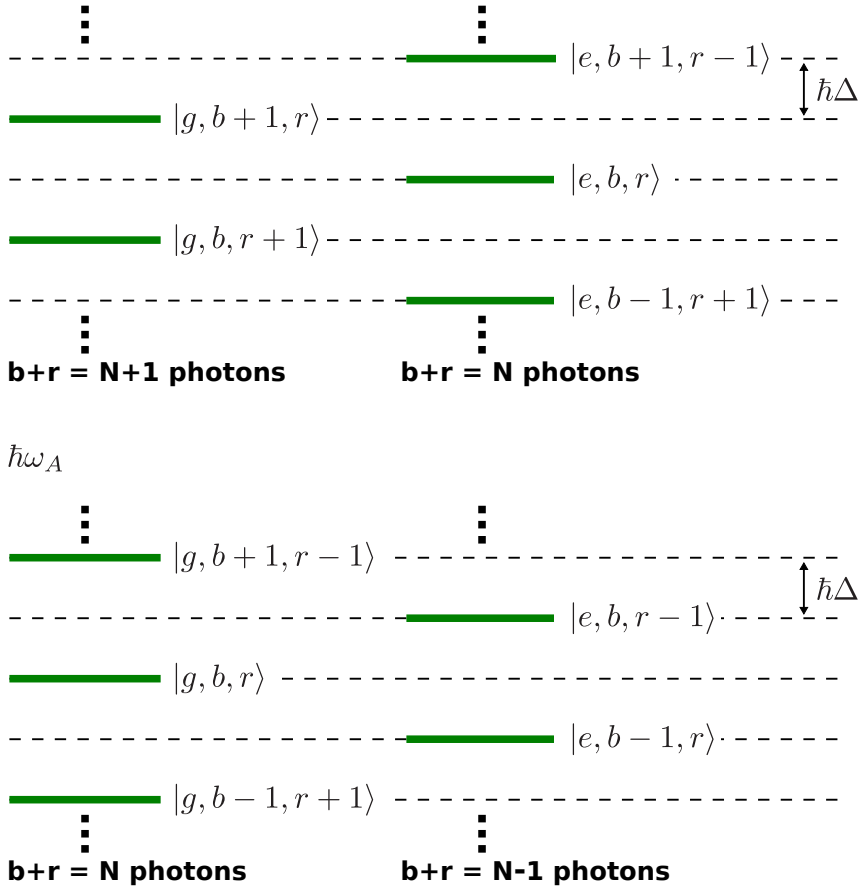

Figure 2.3: The uncoupled product states $|g, b, r\rangle$ and $|e, b, r\rangle$ with different photon distributions. Their energy levels form a ladder of states each separated by $\Delta E = \hbar\Delta$. The manifolds with a different total photon number are separated by the atomic resonance $\hbar\omega_A$. Due to the detuning, the energy levels are not degenerated as in Figure 1.5.

three-dimensional basis $\{|e, b-1, r\rangle, |g, b, r\rangle, |e, b, r-1\rangle\}$ leads to:

$$\begin{aligned}\hat{H}_{int} = &\frac{\hbar\tilde{\Omega}_b}{2}\left(\hat{a}_b^\dagger|g, b, r\rangle\langle e, b, r| + \hat{a}_b|e, b, r\rangle\langle g, b, r|\right) \\ &+ \frac{\hbar\tilde{\Omega}_r}{2}\left(\hat{a}_b^\dagger|g, b, r\rangle\langle e, b, r| + \hat{a}_b|e, b, r\rangle\langle g, b, r|\right)\end{aligned} \tag{2.6}$$

The coupling parameters $\Omega_{b,r}$ are given by the light field configuration. By re-grouping same frequency terms, the electric fields in (2.1) yield the standing waves [27]:

$$E = 2E_0\cos(kz + \frac{\Delta\phi}{4})\cos([\omega_A + \Delta]t) + 2E_0\cos(kz - \frac{\Delta\phi}{4})\cos([\omega_A - \Delta]t) \tag{2.7}$$

Here, $\Delta\phi$ is the relative phase difference of the electric fields. With this, the position-dependent coupling parameters are [27]:

$$\Omega_{b,r}(z) = 2\Omega \cos(kz \pm \frac{\Delta\phi}{4}) \tag{2.8}$$

In this case, the total Hamiltonian is also position-dependent and can be written in matrix form using the non-coupled states as basis. Truncated to 7×7 for simplicity, it is then:

$$\hat{H}_{tot} = (b+r)\hbar\omega_A \cdot \mathbb{1}_7 + \hbar \begin{pmatrix} 3\Delta & \frac{\Omega_r}{2} & 0 & 0 & 0 & 0 & 0 \\ \frac{\Omega_r}{2} & 2\Delta & \frac{\Omega_b}{2} & 0 & 0 & 0 & 0 \\ 0 & \frac{\Omega_b}{2} & \Delta & \frac{\Omega_r}{2} & 0 & 0 & 0 \\ 0 & 0 & \frac{\Omega_r}{2} & 0 & \frac{\Omega_b}{2} & 0 & 0 \\ 0 & 0 & 0 & \frac{\Omega_b}{2} & -\Delta & \frac{\Omega_r}{2} & 0 \\ 0 & 0 & 0 & 0 & \frac{\Omega_r}{2} & -2\Delta & \frac{\Omega_b}{2} \\ 0 & 0 & 0 & 0 & 0 & \frac{\Omega_b}{2} & -3\Delta \end{pmatrix} \tag{2.9}$$

The second term of this Hamiltonian is the interaction term [30] and the matrix can be diagonalized. The position-dependent eigenvalues are the energy levels of the coupled system.

Figure 2.4 shows the energy levels and the intensity of the standing waves for different positions with $\Delta\phi = \pi$ and Rabi frequency $\Omega = \frac{\pi}{4}\Delta$. Avoided crossings of two levels occur at certain positions, but an atom moving with non-zero velocity v can make Landau-Zener transitions through them [31]. The probability for this process is:

$$P_{LZ} = \exp\left(\frac{-\pi U^2}{\hbar v \nabla E}\right) \tag{2.10}$$

Here, U is the energy difference between two levels and ∇E the gradient of the energy. The probability for a Landau-Zener transition therefore gets higher for smaller gaps and larger slopes. $P_{LZ} \approx 1$ at the avoided crossings and the atom will tunnel nearly every time, losing kinetic energy in this process by climbing up or gaining kinetic energy by

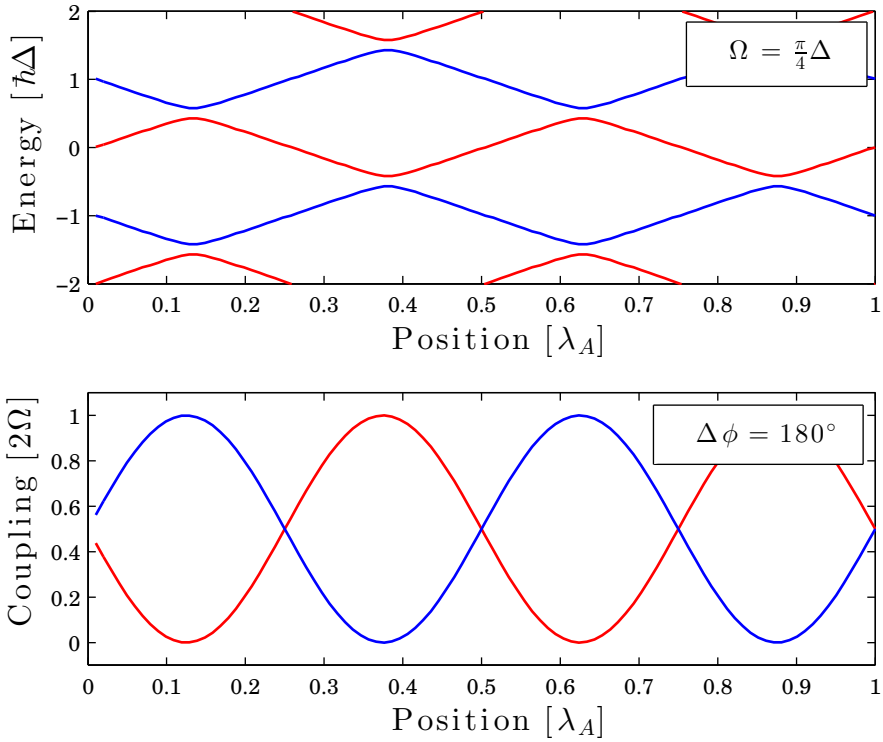

Figure 2.4: The diagram shows the energy levels of the dressed states for Rabi frequency $\Omega = \frac{\pi}{4}\Delta$ and relative phase difference $\Delta\phi = \pi$ of the standing waves. In this model, a moving atom can make Landau-Zener transitions with the probability given in (2.10), which are most likely at the avoided crossing. The atom climbs the infinite ladder of dressed states and loses kinetic energy due to this coherent process.

falling down the infinite ladder of dressed states.

In this model, spontaneous emissions are dissipative losses of the light field energy and will change the sign of the slope. For a symmetric phase difference of $\Delta\phi = \pi$, the time and spatial average of the force is zero as in the π-pulse model. Again, a different choice of relative phase leads to a non-vanishing force. The energy gaps between two levels vary with change of the relative phase difference and another minimum occurs at $\Delta\phi = \frac{\pi}{2}$. This has also been used as the optimum phase in the π-pulse model of the previous section.

Figure 2.5 shows the dressed states with relative phase difference $\Delta\phi = \frac{\pi}{2}$. In contrast to the π-pulse model, the energy gaps at nodes of one of the standing waves are minimal

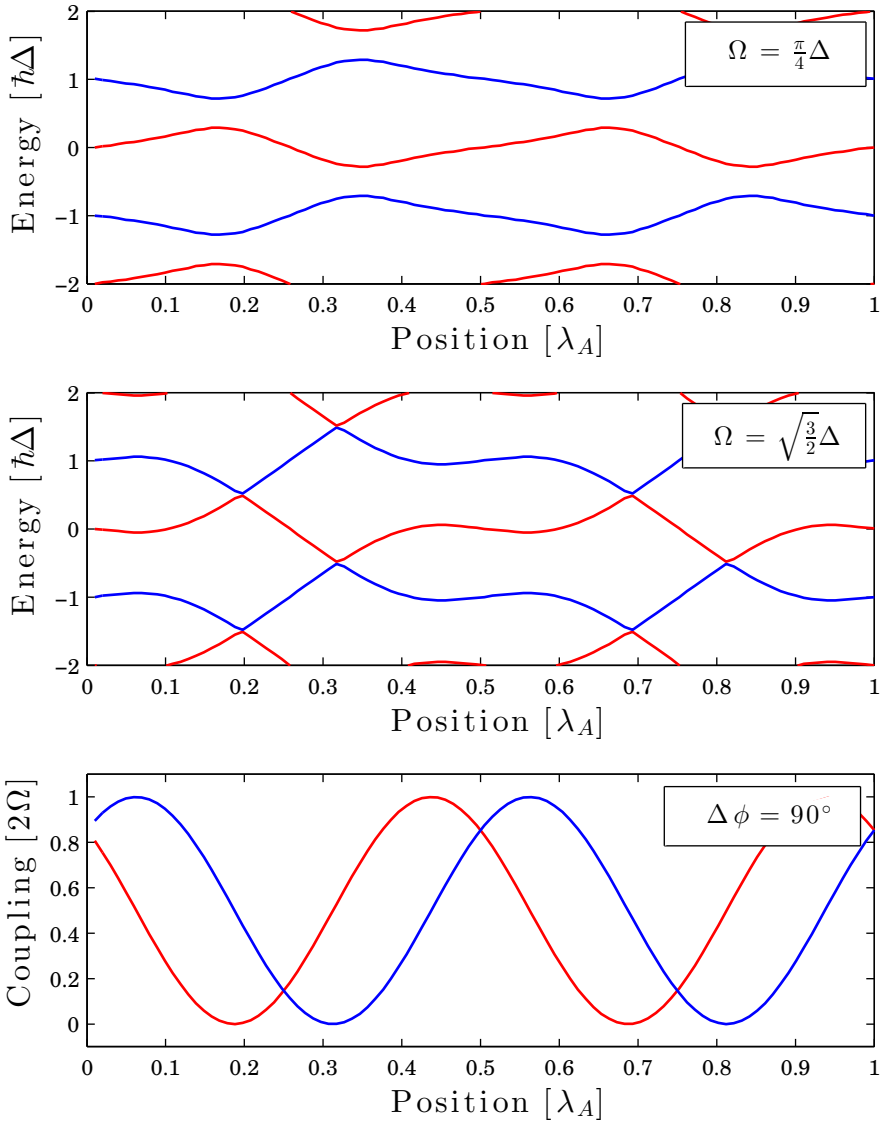

Figure 2.5: The energy levels of the dressed states for a relative phase difference $\Delta\phi = \frac{\pi}{2}$, where the energy gaps between two levels have another minimum. In contrast to $\Omega = \frac{\pi}{4}\Delta$ of the π-pulse model, the smallest gap can be achieved with $\Omega = \sqrt{\frac{3}{2}}\Delta$.

for a Rabi frequency of $\Omega = \sqrt{\frac{3}{2}}\Delta$. Spontaneous emissions will occur more likely in the levels that have a larger admixture of the excited state, so that depending on the sign of the relative phase, an upward or downward path through the ladder of dressed states is preferred on average.

The dressed states with the largest mixture of the uncoupled excited states are shown as bold lines in Figure 2.6. Due to the asymmetric phase difference of the standing waves,

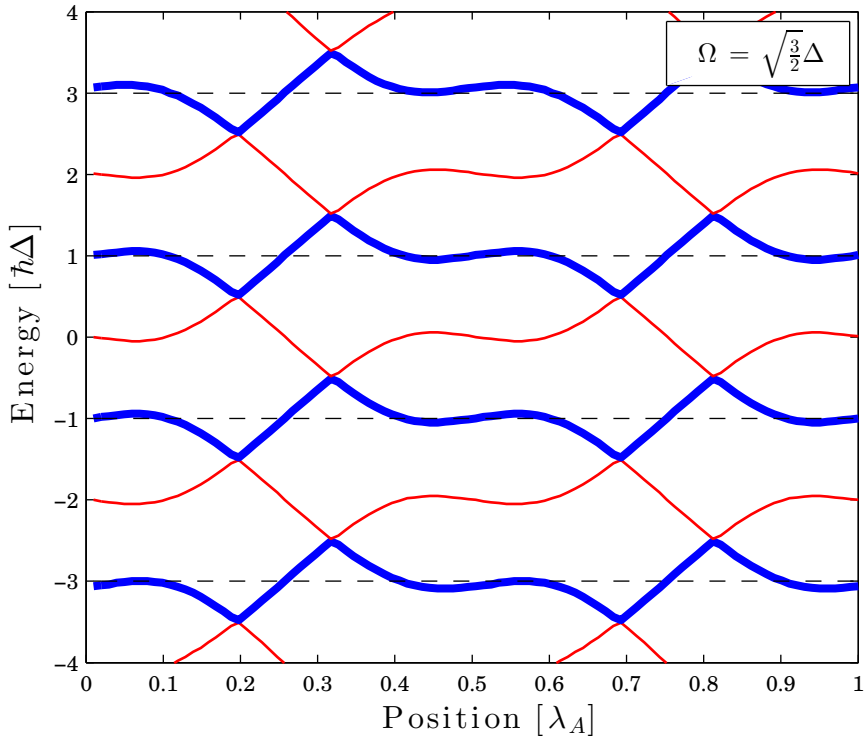

Figure 2.6: The bold energy levels have larger mixture with the uncoupled excited states, which are shown by the dashed lines. Spontaneous emission occurs more likely in these states, so that in this case, the atom will follow an upward path on average. A sign reversal in the relative phase difference of the standing waves will prefer a mean downward path.

the atom will lose its kinetic energy in 75% of the time and gain kinetic energy in 25% of the time, resulting in an average force [30]:

$$F_{BC,DDA} = \frac{3}{4}|\frac{\Delta E}{\Delta z}| - \frac{1}{4}|\frac{\Delta E}{\Delta z}| = \frac{\hbar k \Delta}{\pi} \tag{2.11}$$

Here, the detuning Δ is the same as shown in Figures 2.4 - 2.6. This gives the same force as in the π-pulse model, but with a larger optimal Rabi frequency $\Omega = \sqrt{\frac{3}{2}}\Delta \approx 1.6 \cdot \Omega_\pi$.

A more detailed analytical solution on the optimal Rabi frequency and relative phase difference is provided in [30], where the use of a Floquet Hamiltonian removes the time-dependence of the system. The lower and upper bounds of the velocity range can be explained qualitatively by the Dressed State model, since a minimal velocity is necessary for the atom to move through the states. If velocities are too large, additional Landau-

Zener transitions can occur which will decrease the average force. However, in the scope of this work, the velocity range of the bichromatic force is calculated with the numerical calculation using optical Bloch equations that is presented in the next section.

2.3 Numerical Calculations

The presented models give good understanding on the nature of the bichromatic force, but an exact numerical solution using optical Bloch equations provides far more details, which are needed for experiments.

The optical Bloch equations (1.22) have only three independent parameters, if the overall phase is ignored. These can be expressed by the Bloch vector $\vec{R} = (r_1, r_2, r_3)$, whose components are defined as [22]:

$$r_1 = c_g c_e^* = \rho_{ge} e^{-i\omega t} + \rho_{eg} e^{i\omega t} \tag{2.12a}$$

$$r_2 = i(c_g c_e^* - c_g^* c_e) = i(\rho_{ge} e^{-i\omega t} - \rho_{eg} e^{i\omega t}) \tag{2.12b}$$

$$r_3 = |c_e|^2 - |c_g|^2 = \rho_{ee} - \rho_{gg} \tag{2.12c}$$

The four components of the density matrix ρ defined in (1.20) can be expressed by the components of the Bloch vector $\vec{R}$:

$$\rho_{gg} = \frac{1}{2}(1 + r_3) \tag{2.13a}$$

$$\rho_{ge} = \frac{1}{2}(r_1 - i r_2) e^{i\omega t} \tag{2.13b}$$

$$\rho_{ee} = 1 - \rho_{gg} \tag{2.13c}$$

$$\rho_{eg} = \rho_{ge}^* \tag{2.13d}$$

Inserting this into the optical Bloch equations (1.22) gives the equation of motion for the Bloch vector. When the electric field configuration (2.7) and the definition of the Rabi frequency (1.7) are used, the coupled differential equations for the components of the

Bloch vector are [27, 32]:

$$\dot{r}_1 = -\Delta r_2 - \frac{\gamma}{2} r_1 - 4\Omega r_3 \sin(kvt) \sin(\frac{\Delta\phi}{4}) \sin(\Delta t) \tag{2.14a}$$

$$\dot{r}_2 = -\Delta r_1 - \frac{\gamma}{2} r_2 + 4\Omega r_3 \cos(kvt) \cos(\frac{\Delta\phi}{4}) \cos(\Delta t) \tag{2.14b}$$

$$\dot{r}_3 = \gamma(1 - r_3) + 4\Omega[r_1 \sin(kvt) \sin(\frac{\Delta\phi}{4}) \sin(\Delta t) - r_2 \cos(kvt) \cos(\frac{\Delta\phi}{4}) \cos(\Delta t)] \tag{2.14c}$$

Here, γ is the spontaneous decay rate, Δ the detuning of the frequencies and $\Delta\phi$ the relative phase difference of the standing waves. A velocity dependence is included by the position of the atom due to the substitution $z = vt$. The force for a given velocity v can be calculated as in (1.25) and is found to be [27, 32]:

$$F = 2\hbar k\Omega \left[-r_1 \sin(kvt) \cos(\frac{\Delta\phi}{4}) \cos(\Delta t) + r_2 \cos(kvt) \sin(\frac{\Delta\phi}{4}) \sin(\Delta t) \right] \tag{2.15}$$

The components r_1 and r_2 of the Bloch vector can be calculated numerically from (2.14), if the parameters γ, Δ, Ω, $\Delta\phi$ and the velocity v are given. In this work, *ode23* is used [33].

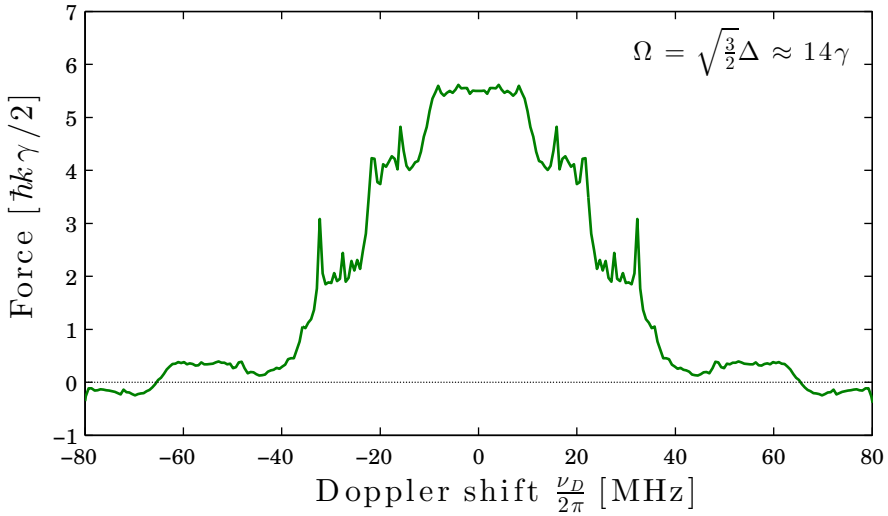

Figure 2.7: The force profiles dependent on the detuning of the atomic resonance calculated with the optical Bloch equations. Here, the parameters for ^{40}Ar, $\gamma = 2\pi \cdot 5.87$ MHz, $\Delta = 2\pi \cdot 65$ MHz $\approx 11\gamma$ and $\Omega = \sqrt{\frac{3}{2}}\Delta \approx 14\gamma$ are used. The sharp resonances corresponds to Doppleron resonances [34] and ordinary optical molasses can be seen at $|\pm kv| = \Delta$.

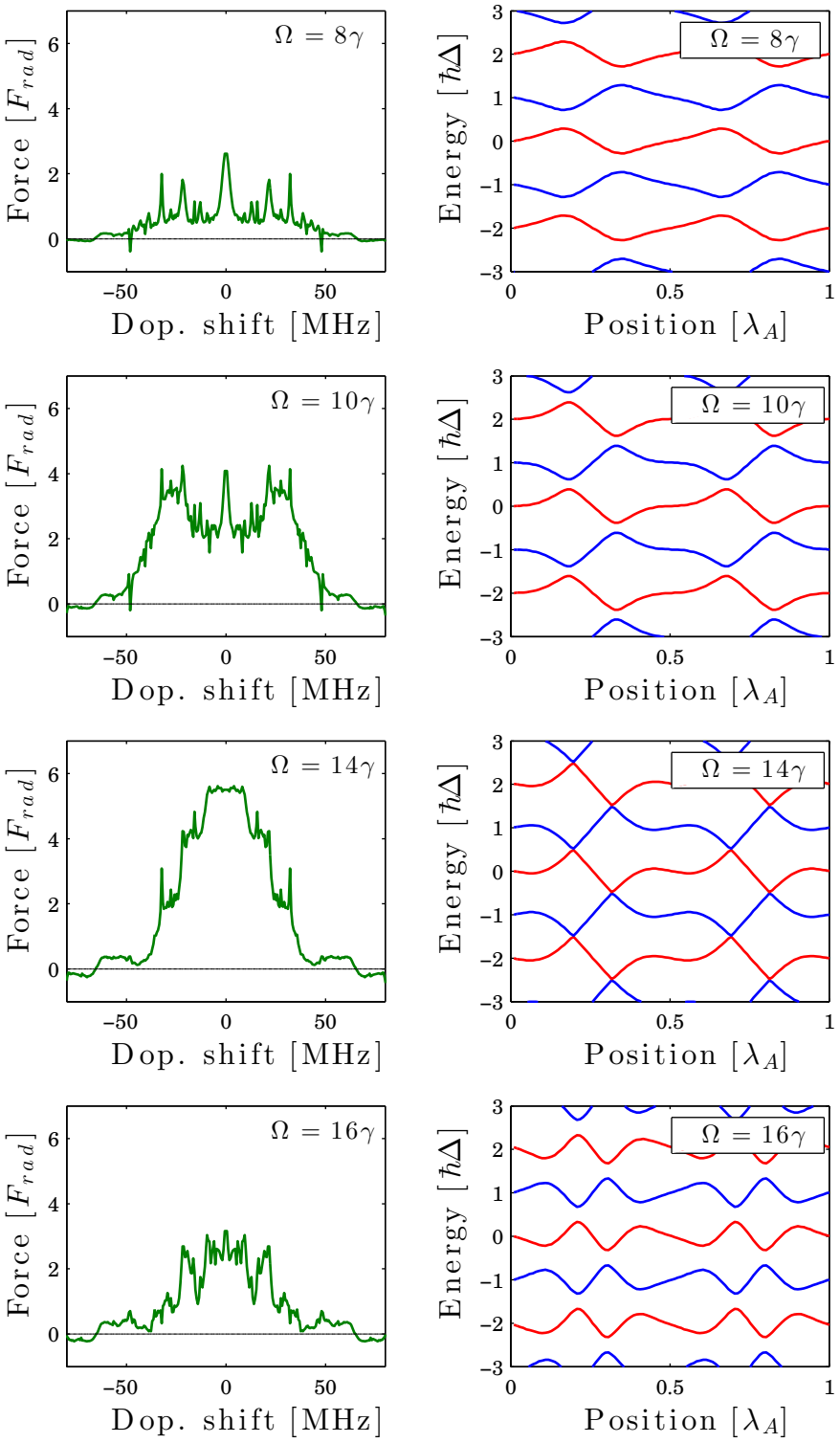

Figure 2.8: The numerically calculated force profiles on the left side with $\Delta = 2\pi \cdot 65$ MHz, $\gamma = 2\pi \cdot 5.87$ MHz and different Rabi frequencies Ω. The dressed states with the same parameters are on the right side. In the scope of the Dressed State model, non-optimal Rabi frequencies $\Omega \neq \sqrt{\frac{3}{2}}\Delta \approx 14\gamma$ result in too large energy gaps or additional gaps for $\Omega \gg 14\gamma$ where undesired Landau-Zener transitions occur.

Figure 2.7 shows the calculated velocity-dependent force profile with $\gamma = 2\pi \cdot 5.87$ MHz for the $1s_5 \rightarrow 2p_9$ transition of ^{40}Ar, $\Delta = 2\pi \cdot 65$ MHz$\approx 11\gamma$, and a Rabi frequency $\Omega = \sqrt{\frac{3}{2}}\Delta \approx 14\gamma$, which are parameters that can be achieved with the experimental setup. The profile shows resonances at certain detunings, which can be explained by Doppleron resonances [34]. Ordinary optical molasses can be seen at Doppler shifts $|\pm kv| = \Delta = 2\pi \cdot 65$ Mhz, since the detuned atom is on-resonance with the single frequencies $\omega_A + \Delta$ from one side and $\omega_A - \Delta$ from the other side.

The numerical calculated maximal force $F_{BC,num} \approx 5.5 F_{rad,max}$ is smaller than the ideal force $F_{BC,DDA} = \frac{\hbar k \Delta}{\pi} = \frac{2}{\pi}\frac{\Delta}{\gamma} F_{rad,max} \approx 7 F_{rad,max}$ calculated by the Dressed State model with the same parameters as above. The difference can be explained by additional Landau-Zener transitions through the dressed states, which always have a non-zero probability and are not taken into account in the force calculation of the dressed states in (2.11).

Figure 2.8 compares the calculated force profiles with the same detuning Δ and spontaneous decay rate γ, but different Rabi frequencies Ω to the dressed states calculated with the same parameters. A lower force with non-optimal Rabi frequency $\Omega \neq \Omega_{opt} = \sqrt{\frac{3}{2}}\Delta$ can be explained in the scope of the Dressed State model by large energy gaps which hinder Landau-Zener transitions for too small Rabi frequencies or undesired Landau-Zener transitions at additional gaps, if the Rabi frequency is too high.

Figure 2.9 shows the calculated phase dependence of the on-resonance bichromatic force with Rabi frequency $\Omega = \sqrt{\frac{3}{2}}\Delta \approx 14\gamma$. The absolute value of the force is maximal for relative phase differences $\Delta\phi = \pm\frac{\pi}{2} = \pm 90°$. In the case of symmetric or antisymmetric phase differences $\Delta\phi = n\pi$ where n is an integer value, the force vanishes as expected from the π-pulse model and the Doubly Dressed Atom model.

The numerical calculation by solving the optical Bloch equations gives the most accurate numbers on the bichromatic force, but it makes certain idealized assumptions. The Rabi frequency Ω of the light field is not spatially constant in real experimental setups

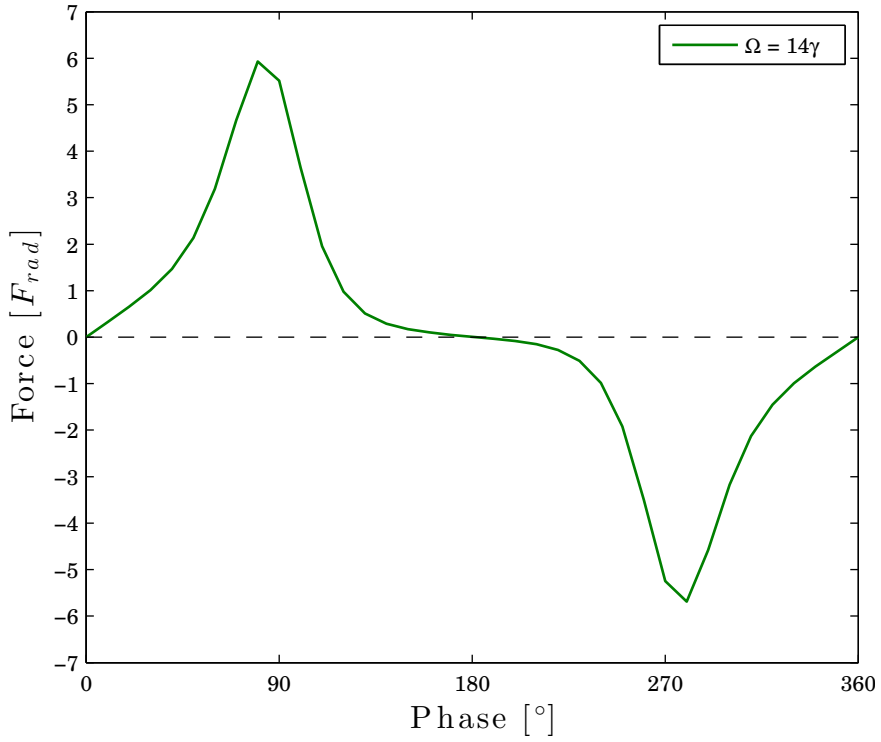

Figure 2.9: The phase dependence of the bichromatic force with optimal Rabi frequency $\Omega = \sqrt{\frac{3}{2}}\Delta \approx 14\gamma$. As expected, the absolute value of the force is largest at $\Delta\phi = \pm\frac{\pi}{2} = \pm 90°$ and is zero in the symmetric or antisymmetric case.

due to the Gaussian intensity distribution of the laser beams so that real measured force profiles will be different from the presented calculated ones.

The next section provides modified calculations considering the changing Rabi frequency for atoms travelling perpendicular to the beam direction. These calculations will be used for comparison of theory and experiment instead of the basic calculations of this chapter.

2.4 Corrections for Gaussian Laser Beams

The idealized light fields of the previous chapters can not be achieved in the experimental setup due to the wave property of light that has to be taken into account. The complex electric field $\vec{U}$ has to fulfill the Helmholtz equation [35]:

$$\nabla^2\vec{U} + k^2\vec{U} = 0 \tag{2.16}$$

Here, $k = \frac{2\pi}{\lambda} = \frac{\omega}{c}$ is the wave vector. The equation (2.16) can be solved by simple monochromatic planar or spherical waves. Although the plane wave with $\vec{U} = \vec{U}_0 e^{-ikz}$ has a constant mean intensity, it is not possible in practice due to the confined space of real laser beams. A general non-radial symmetric solution of the Helmholtz equation is given by Hermite-Gaussian modes [35] that can be used to describe the output of laser cavities with different horizontal and vertical geometries. The symmetric zeroth order of these modes is called Gaussian beam and is given by:

$$U(\rho, z) = U_0 \frac{\mathrm{w}_0}{\mathrm{w}(z)} \exp\left(\frac{-\rho^2}{w(z)^2}\right) \exp\left(-ikz - ik\frac{\rho^2}{2R(z)} + i\zeta(z)\right) \tag{2.17}$$

Here, w_0 is the beam waist, $\mathrm{w}(z) = \mathrm{w}_0\sqrt{1 + (\frac{z}{z_R})^2}$ is the radius of the beam at position z with Rayleigh range $z_R = \frac{\pi \mathrm{w}_0^2}{\lambda}$, $R(z) = z[1 + (\frac{z_0}{z})^2]$ is the curvature of the wavefronts, $\zeta(z) = \tan^{-1}(\frac{z}{z_0})$ is the additional Gouy phase and $\rho = \sqrt{x^2 + y^2}$ is the axial distance.

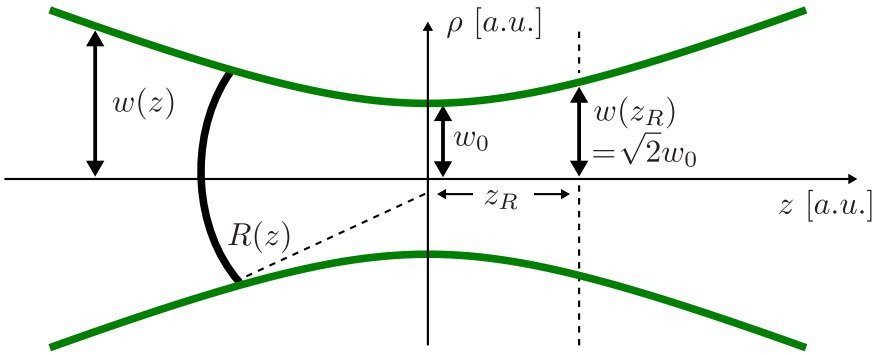

Figure 2.10: Schematic diagram of a Gaussian beam in the ρz-plane, with the distance $\rho = \sqrt{x^2 + y^2}$ to the z-axis, the position-dependent beam radius $\mathrm{w}(z)$, beam waist $\mathrm{w}_0 = \mathrm{w}(0)$ and Rayleigh range z_R, where the surface of the beam cross section is doubled. The radius of the wave front curvature is given by $R(z) = z[1 + (\frac{z_0}{z})^2]$

Figure 2.10 shows a schematic diagram of a Gaussian beam with the relevant parameters. Near the light source, $z \ll z_R$ and the curvature is $R \to \infty$ so the wavefronts are nearly planar and for long distances $z \gg z_R$, they are spherical with $R \to 1$. The intensity at

position ρ and z is given by:

$$I(\rho,z) = |U(\rho,z)|^2 = I_0(\frac{\mathrm{w}_0}{\mathrm{w}(z)})^2 \mathrm{exp}(-\frac{2\rho^2}{\mathrm{w}(z)^2}) \approx I_0 \mathrm{exp}(-\frac{2\rho^2}{\mathrm{w}_0}) \tag{2.18}$$

The approximation in the last part of the equation can be made, since $z \ll z_R$ in the experimental setup of this work and the collimated beam radius can be seen as constant.

The upper graph in Figure 2.11 shows the intensity distribution in the xy-plane for a Gaussian laser beam in the z-direction. The lower graph shows the intensity for an atom travelling in x-direction perpendicular to the beam with two different values of y, one through the center of the beam and the other half a beam radius w_0 away from the center. The difference in the intensity is significant and this also has to be considered in further force calculations.

Discretization of the intensity profile has to be made for solving the optical Bloch equations. For simplicity, the intensity profile is rounded to 10% steps as shown by the discrete lines in Figure 2.11 and the Rabi frequency can be calculated by (1.23).

For an atom travelling with constant longitudinal velocity v_{long} through a laser beam in transverse direction with diameter $d = 2\mathrm{w}_0$, the total perpendicular force

$$F_{z,tot} = m \sum_n a_{trans,n} = \frac{m v_{long}}{d} \sum_n v_{trans,n} = \frac{m v_{long}}{2\mathrm{w}_0} v_{trans,tot} \tag{2.19}$$

is proportional to the total change of velocity $v_{trans,tot}$ in transverse direction. With a beam intensity $I_0 = 3I_S(\frac{\Delta}{\gamma})^2$ where $\Delta = 2\pi \cdot 65$ MHz and $\gamma = 2\pi \cdot 5.87$ MHz as in the previous chapter, the velocity shifts can be calculated using the bichromatic force profiles from the optical Bloch equation.

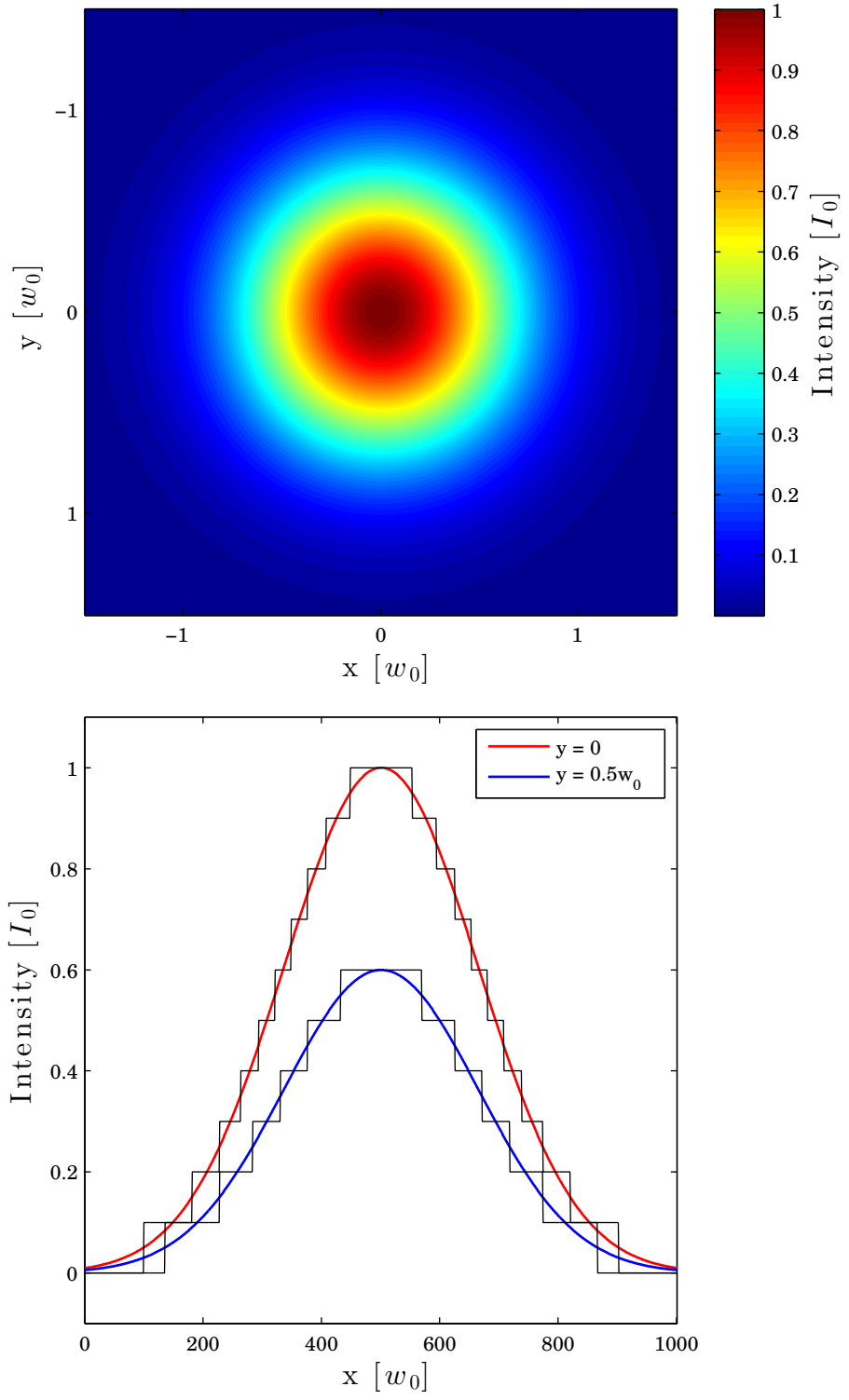

Figure 2.11: The upper figure shows the profile of a Gaussian beam at $z = 0$. The beam waist is w_0 and defines the distance to the axis where the intensity is reduced to $I(w_0) = \frac{1}{e^2} I_0$. The intensities at two cross-sections with $x = 0$ and $x = \frac{w_0}{2}$ is shown in the lower picture. For simplicity, the discrete lines with 10% intensity steps can be used for the Rabi frequencies in the optical Bloch equations.

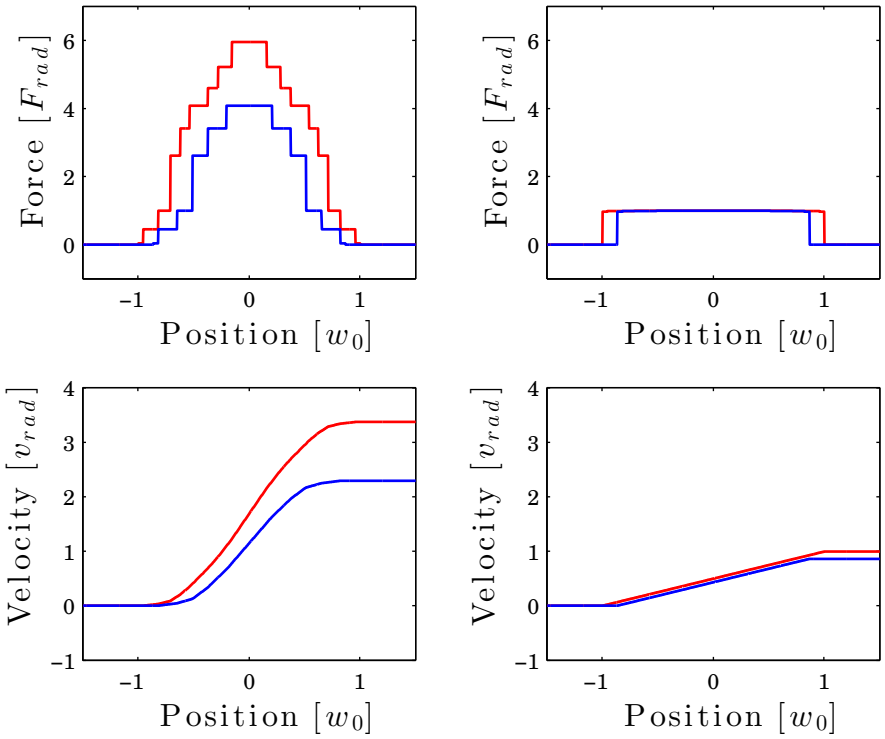

Figure 2.12: On the left side are the bichromatic forces and resulting velocity changes for an atom travelling perpendicular to the beams with constant v_{long}. The same intensity distribution is used for the radiative force and velocity change on the right side. The diagrams are normalized to the maximal radiative force or maximal radiative velocity change through the beam center.

Figure 2.12 shows the perpendicular forces on an atom travelling through the interaction region of the laser beams and the resulting velocity change. The bichromatic force for non-optimal Rabi frequencies due to the different intensities is significantly smaller whereas the radiative force is nearly saturated on the whole beam cross section.

The optical power P is easier to handle experimentally than the intensity and is connected to the latter by:

$$P = \int_A I(\rho, z) dA \tag{2.20}$$

Using $A = \pi \mathrm{w}_0^2$ as integration surface, the optical power can be chosen to maximize the total force (2.19).

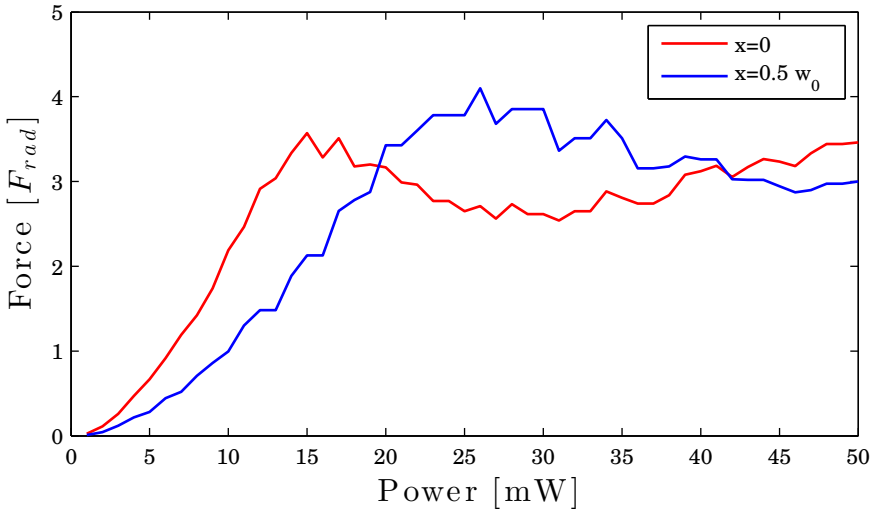

Figure 2.13: The bichromatic force for the same detuning Δ but different power values calculated with the optical Bloch equations using the Gaussian beam corrections presented in this chapter. The lines show two paths of the atom with distances $x = 0$ and $x = \frac{w_0}{2}$ from the laser beam center. The mean force is saturating for higher power in contrast to the optimal power of the non-corrected models.

Figure 2.13 shows the total on-resonance bichromatic force on an atom travelling perpendicular through the laser beams for two distances from the beam axis and different values of the optical power. For a laser beam with the same cross section, but a constant intensity, the Dressed State model gives a power optimum of $P = IA = 3I_S \pi w_0^2 \frac{\Delta^2}{\gamma^2}$. The maximal force considering Gaussian beams is at larger power values, since the optimal Rabi frequency can not be achieved everywhere.

The corrections have not considered Doppler shifting of the atomic resonance by recoil of photons due to stimulated emission. The angle of the atomic path to the laser beams will also change, so that the longitudinal velocity v_{long} has an influence on the Doppler shift, especially for misalignments.

Figure 2.14 shows the bichromatic force profile with $w_0 = 1$ mm, $P = 50$ mW, $\gamma = 2\pi \cdot 5.87$ MHz, $\Delta = 2\pi \cdot 65$ MHz and a longitudinal velocity $v_{long} = 274 \frac{m}{s}$. Including the corrections mentioned above, the force is significantly smaller than the idealized calculations of the previous sections. In contrast to the radiative force, the bichromatic force

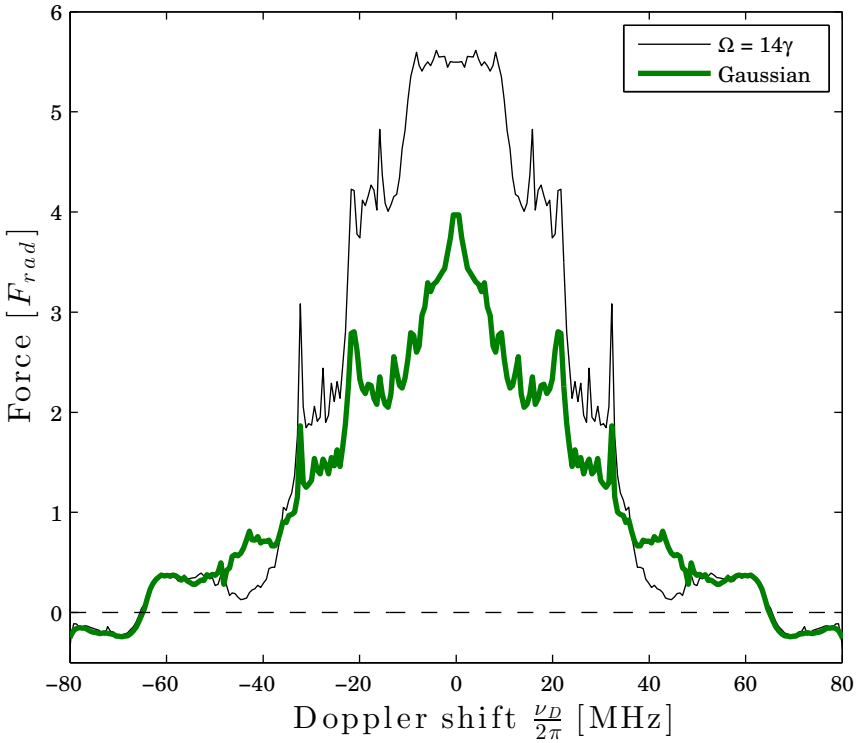

Figure 2.14: The bichromatic force profile calculated with the optical Bloch equations and corrected with Gaussian beams is shown as bold curve. The parameters are $w_0 = 1$ mm, $P = 50$ mW, $\gamma = 2\pi \cdot 5.87$ MHz, $\Delta = 2\pi \cdot 65$ MHz and a longitudinal velocity $v_{long} = 274\frac{m}{s}$. The non-corrected force profile from the previos chapter is shows as thin curve.

is not limited fundamentally and larger forces can be achieved with higher detunings Δ, if enough laser power is available. In the scope of this work, a maximum power of 50 mW is used.

Figure 2.15 shows the phase dependence of the bichromatic force calculated with the basic theory of the last section and compared to the theoretical curve acquired with the corrections mentioned in this section. A power of $P = 50$ mW is used for the corrected theoretical curve. As expected, the force is lower due to the changing Rabi frequency of a Gaussian laser beam. Additionally, the phase dependence is broader than in the basic calculations.

For the comparison of theory and experiment, the basic theoretical calculations of the last section have to be corrected with the Gaussian beam profile since this leads to very

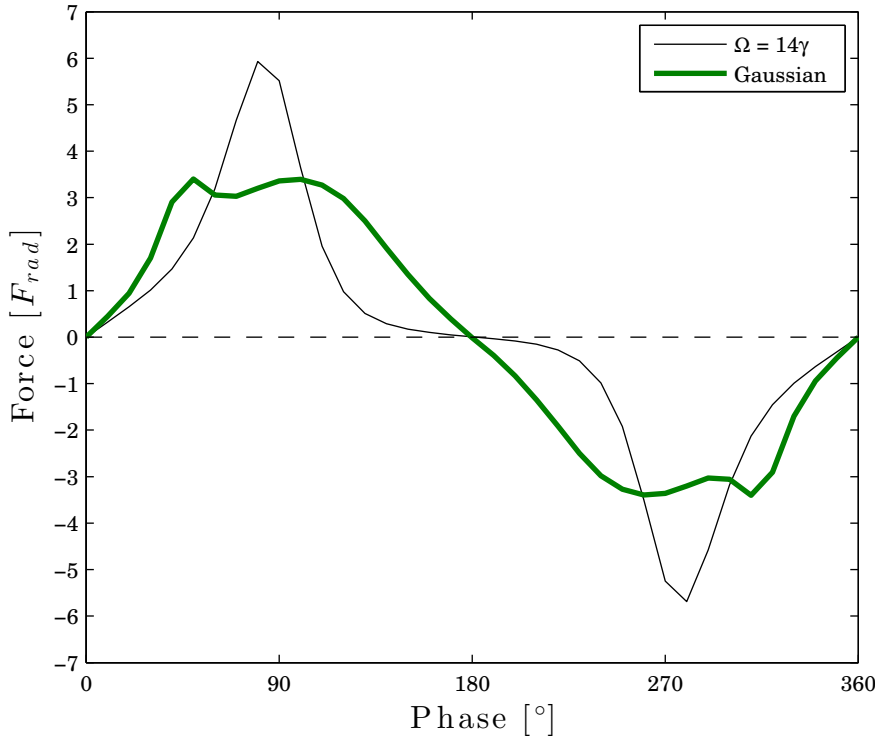

Figure 2.15: The phase dependences of the bichromatic force with optimal Rabi frequency compared to the calculations with $P = 50$ mW using Gaussian beam profile corrections. As expected from the previous calculations, the maximal force is significantly smaller. Additionally, the phase dependence is broader than in the basic calculations.

different results. In the scope of this work, all further used theoretical curves are including the corrections that have been described in this chapter.

Chapter 3

Experimental Setup

The experimental setup for creating and measuring the bichromatic force on ^{40}Ar atoms is presented in this chapter. The optical frequency generation with subsequent amplification is described in the first two sections. The last section shows the setup for the interaction of these frequencies with a collimated beam of metastable argon and describes the measuring method of the bichromatic force in this work. The ATTA-apparatus used in the scope of this work is only briefly mentioned since it is well documented in previous publications of the work group [5, 16, 18--21].

3.1 Four-Frequency Generation

In the simple case of atoms with zero velocity, the bichromatic force needs two counter-propagating beams each with frequencies detuned by $\pm\Delta$ from resonance ω_A. For atoms moving with a velocity v_{trans} in beam direction, the frequencies have to be corrected with the Doppler shift $\nu_D = -kv_{trans}$ to be on atomic resonance again. Therefore, the general four frequencies required for bichromatic forces are:

$$\nu_{BCF} = \begin{cases} \omega_A + kv_{trans} \pm \Delta & \text{for } 1^{\text{st}} \text{ beam} \\ \omega_A - kv_{trans} \pm \Delta & \text{for } 2^{\text{nd}} \text{ beam} \end{cases} \tag{3.1}$$

In each of the models presented in the last chapter, a defined relative phase difference of the frequencies is necessary. Changing the phase of the beat nodes will change the

phase of the beating in the π-pulse model or the phase difference of the standing waves in the Dressed State model.

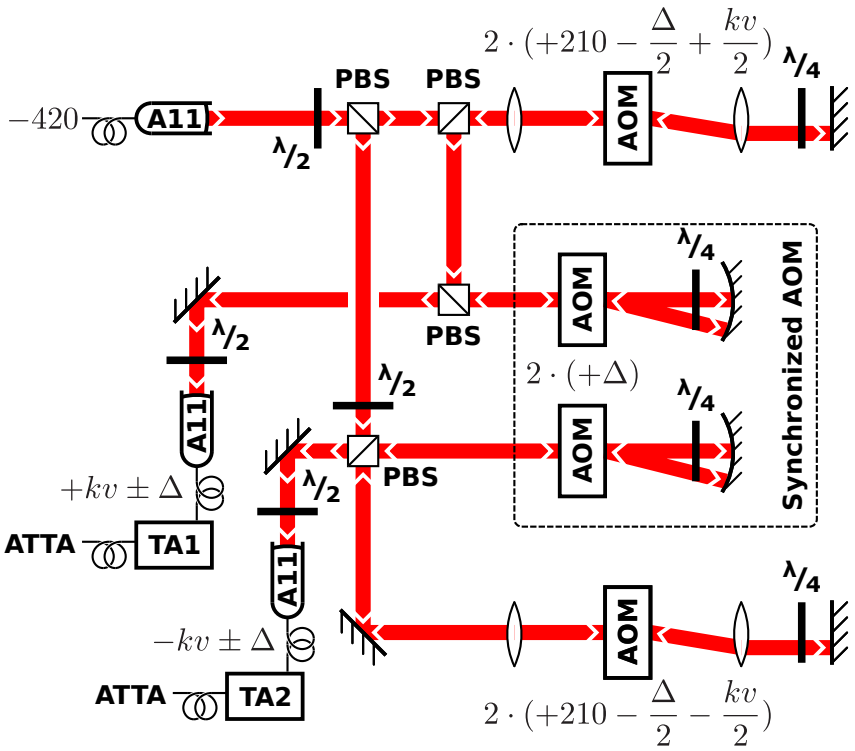

Figure 3.1: Schematic diagram of the optical setup for generation of the necessary frequencies, given in units of MHz in relation to the atomic resonance ω_0. The incoming light has a detuning of -420 Mhz and is shifted upward to $-\Delta \pm kv$ with the top and the bottom AOM. The two AOM's in the middle are driven by synchronized frequency generators such that a relative phase shift can be adjusted. The zeroth order and doubly passed first order are added together to the resulting four frequencies $\nu_{BCF} = \omega_A \pm kv_{trans} \pm \Delta$.

Figure 3.1 shows a schematic diagram of the setup that generates the required four frequencies that are required. The incoming light from the main experiment is detuned by -420 MHz from atomic resonance ω_A due to the given optical setup [20]. The top and bottom doubly passed Acousto-Optical Modulators (AOM) shift the frequencies to $-\Delta \pm kv$. In the scope of this work, the force is acting on a collimated beam of metastable argon atoms [19], so that v_{trans} has a narrow velocity distribution $\sim \pm 10 \frac{\mathrm{m}}{\mathrm{s}}$ around zero. Therefore, the lowest AOM was not present in earlier stages of this experiment and was added for measurements on the detuned force profiles with $kv \neq 0$.

The second frequency component is added to the two Doppler shifted beams by the AOM's in the middle of Figure 3.1, which are driven by synchronized Agilent 33250A frequency generators with acoustic frequency Δ. The light through these AOM's is distributed equally into the zeroth and first order, so that the four frequencies ν_{BCF} of (3.1) are generated by double passing as shown in [36]. The relative phase of the acoustic waves $\Delta\phi_{AOM}$ can be adjusted with the function generator. This setup will directly change the relative phase $\Delta\phi$ between the zeroth order $(\omega_A - \Delta)$ and the first order $(\omega_A + \Delta)$ of the optical frequencies. A schematic diagram of the relation between acoustic and optical phase is shown in Figure 3.2 for two different acoustic phases.

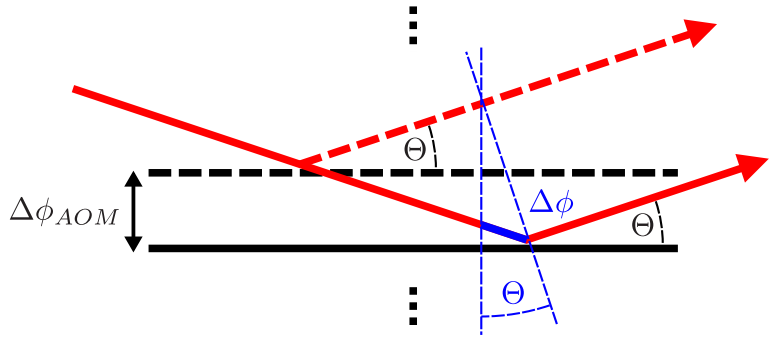

Figure 3.2: Schematic diagram of relation between relative acoustic phase $\Delta\phi_{AOM}$ and the relative optical phase $\Delta\phi$. Here, the horizontal lines are one node of the acoustic density lattice for two different acoustic phases. The light passing through the AOM will gain the same amount of relative phase.

The optical phase will be changed by twice the acoustic phase since the light is passing the AOM two times in this configuration. The zeroth order and the twice diffracted first order beams of each AOM path are coupled into the same optical fiber.

Figure 3.3 shows a measurement of the output signal of the two fibers containing the two frequencies $\omega_A \pm \Delta$ from each path. The phase of these beatings have been adjusted with the phase of the frequencies driving the AOM. The ratio of zeroth and first order beams passing the synchronized AOM's can be quantified with the visibility:

$$\nu_{vis} = \frac{P_{max} - P_{min}}{P_{max} + P_{min}} \tag{3.2}$$

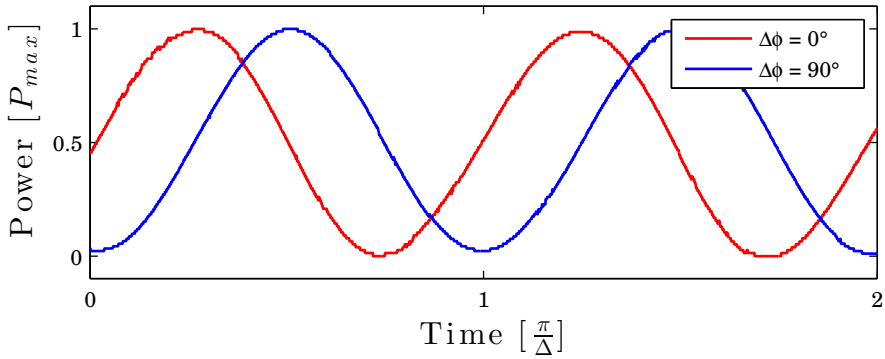

Figure 3.3: The measured output signal of the fibers containing two frequencies $\omega_A \pm \Delta$. The phase relation of both signals is constant and can be adjusted due to the synchronized AOM's. The ratio of zeroth and first order beam can be optimized for maximum visibility $\nu_{vis} = \frac{P_{max}-P_{min}}{P_{max}+P_{min}}$

.

An ideal beating of two frequencies with the same power leads to the visibility $\nu_{vis} = 1$. This is almost the case as can be seen in Figure 3.3. The next section describes the amplification of this signal to achieve the necessary power for the bichromatic force.

An alternative approach to generate the four frequencies is to consider the other diffraction orders. For $kv = \Delta$, a single AOM can provide all frequencies needed for the bichromatic force as shown in [27]. However, these setups require an optical delay line for adjusting the phase. In the scope of this work, the presented solution with two synchronized AOM's is preferred due to its flexibility and instant phase adjustment.

3.2 Tapered Amplifier for Strong Pulse Trains

A strong bichromatic force requires intensities that are much larger than in the case of the radiative force. For a certain detuning Δ, the intensity can be directly calculated from the Rabi frequency condition using the relations given in (1.23):

$$I_{BC} = 2I_S\frac{\Omega^2}{\gamma^2} = 3I_S\frac{\Delta^2}{\gamma^2} \tag{3.3}$$

Here, I_S is the saturation intensity and γ the spontaneous decay rate. The necessary power $P_{BC} = I_{BC} \cdot \pi w_0^2$ is dependent on the beam radius w_0. In the scope of this work,

it is in the order of tens of milliwatt up to a few hundred milliwatt. Since a Gaussian beam has to be considered, the required intensity can be even higher than in (3.3).

The two beams with frequencies $\omega_A \pm kv \pm \Delta$ described in the last section are each coupled into a tapered amplifier (TA). These seed frequencies are amplified in the TA diode due to stimulated emission which was studied in [36] prior to this work. In contrast to ordinary laser diodes, the surfaces of the TA diode are not reflecting and no resonator is formed inside. Therefore, it can be operated with higher currents without permanent damage to the diode. This leads to a large gain of the seed signal.

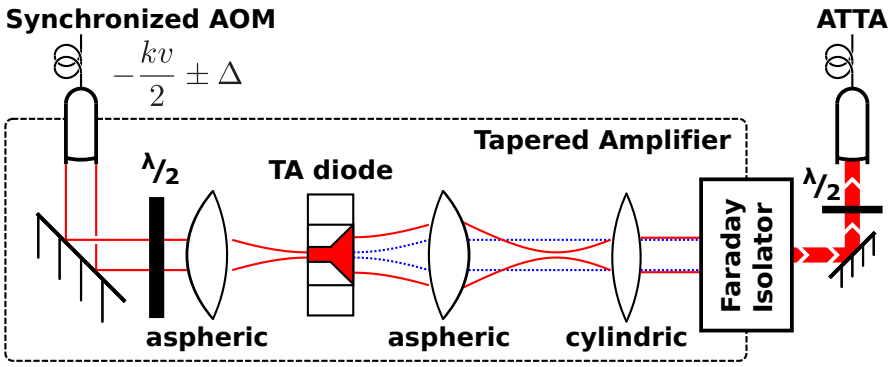

Figure 3.4: Schematic diagram of a tapered amplifier. The fiber docked seed beam is focused with an aspheric lens onto the small facet of the TA diode. The position and angle of the seed can be adjusted with the coupler and the mirror. The aspheric and cylindrical lens behind the diode correct the two axes, so that a collimated beam is formed. An optical isolator prevents retro-reflections from subsequent optics.

Figure 3.4 shows a schematic diagram of the TA used in the experimental setup. They were built and documented in [36, 37] and have been recollimated in the scope of this work. The optics correct asymmetry of the two axes due to the geometry of the TA diode so that a circular and collimated beam leaves the device. An optical isolator prevents retro-reflections from subsequent optics. The amplified frequencies are coupled again into a fiber which leads to the ATTA apparatus.

Figure 3.5 shows the measured output of the fiber behind one of the tapered amplifier for two different powers. The signal for a mean output power of 50 mW is still good, al-

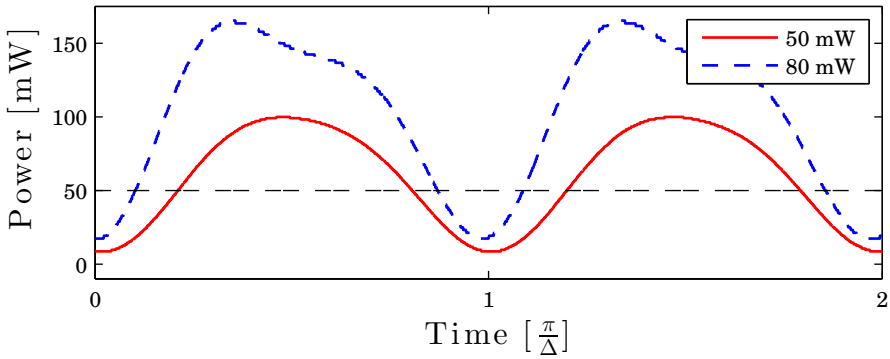

Figure 3.5: Measured amplified output signal in the fiber behind the tapered amplifier. The solid curve is a beating with 50 mW mean power and has a slightly worse visibility than the seed signal due to non-perfect beating and amplified spontaneous emission coupled into the fiber. Increasing the current of the TA diode leads to higher power, but non-linear gain effects occur.

though the visibility is decreased due to non-perfect beating and amplified spontaneous emission coupled into the fiber. For higher power, some non-linear effects occur and the output beating gets worse. This seems to be an individual effect of the different TA diodes, as each of them behaves differently. In the scope of this work, a maximum mean power of 50 mW has not been exceeded.

3.3 Interaction Zone and Detection of the Deflected Atom Beam

The amplified four frequencies of the last section are guided to the ATTA apparatus [16] through two optical fibers. The apparatus gives access to a collimated beam of metastable argon atoms and only few modifications had been necessary to implement the measurement of the transverse bichromatic force.

Figure 3.6 shows a schematic diagram of the experimental setup to deflect the argon beam with the bichromatic force. Documentations on the metastable argon source and transverse collimator can be found in [16], so they are not described further in this work. Modifications on the Magneto-Optical Lens [5] have been made to implement the bichromatic laser beams at its position, since it provides good optical access to the atom beam.

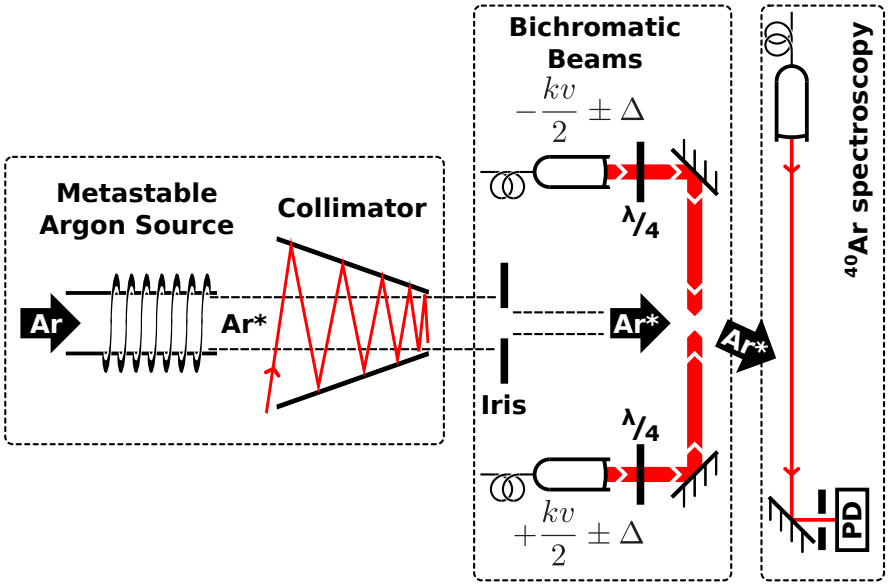

Figure 3.6: Schematic diagram showing the parts of the apparatus used for the measurement of the transverse bichromatic force. The beam is generated with the metastable argon source and collimator and is deflected in the bichromatic interaction region. There, the bichromatic beams are overlapped with the center of the atom beam by the coupler and the mirror. The power has been stabilized by photodiodes behind the mirrors that are not shown here. The deflected argon beam has a transverse detuning that can be detected by an absorption spectroscopy.

The used $1s_5(J = 2) \rightarrow 2p_9(J = 3)$ transition of ^{40}Ar, where the states are given in Paschen-Notation, has different magnetic substates m_J as shown in Figure 1.2. The light of the counter-propagating beams is circularly polarized with the quarter-wave plates to be either σ^+-σ^+ or σ^--σ^- with respect to the atoms. This optically pumps the atoms to the stretched states, so that a two-level system can be obtained.

The laser beams can be overlapped with the couplers and the mirrors shown in Figure 3.6. This has to be adjusted while maintaining superposition with the atom beam at the same time. A good overlap of the two light beams is achieved, when one beam is coupled back into the fiber of the other beam. The optical isolator in front of the tapered amplifier absorbs the retro reflected power. The power of the bichromatic beams has been stabilized by photodiodes behind the mirrors.

The measurement of the bichromatic force is done with an absorption spectroscopy, which is generated by the modulation of the offset-lock frequency of the repumper laser [20] from the existing ^{39}Ar laser system. This provides easy access to an absolute frequency scale. The force deflects the atom beam which gains a transverse velocity v_{trans}, so that the spectroscopy signal is Doppler detuned by:

$$\nu_D = -kv_{trans} = -ka_{trans}t = -k\frac{\bar{F}_z}{m}\frac{d}{v_{long}} \tag{3.4}$$

Here, d is the diameter of the beams and v_{long} the longitudinal velocity of the atoms. For the first adjustments of the bichromatic beams and superposition with the atoms, the atom beam imaging tool [21] was used and an iris was necessary to have a good signal for optimization. The final measurements were taken with the absorption spectroscopy, where the iris has been redundant.

Chapter 4

Measurements of the Bichromatic Force

The bichromatic force on metastable ^{40}Ar has been demonstrated and characterized in the scope of this work by measurements on a collimated atom beam and the results are presented in this chapter. The first part shows qualitative measurements with the atom beam imaging tool [21] which has been very useful for overlapping the laser beams with the atom beam. Quantitative results have been achieved by measurements with an absorption spectroscopy and they are presented in the rest of this chapter.

4.1 Atom Beam Imaging

The atom beam imaging was set up in [21] and has a great value as adjusting and control tool of the ATTA experiment since then. It was used in the early stages of this work for a first signal of the bichromatic force.

The collimated atom beam has a diameter of approximately two centimeters, but since the Schaefter+Kirchhoff 60FC-4-A11-02 coupler used for the laser beams have a diameter of 1.97 mm, a large cross section of the atom beam can not be addressed by the bichromatic force. An iris with 2 mm diameter is used for better resolution and was inserted into the atom beam after the transverse collimation as shown in Figure 3.6.

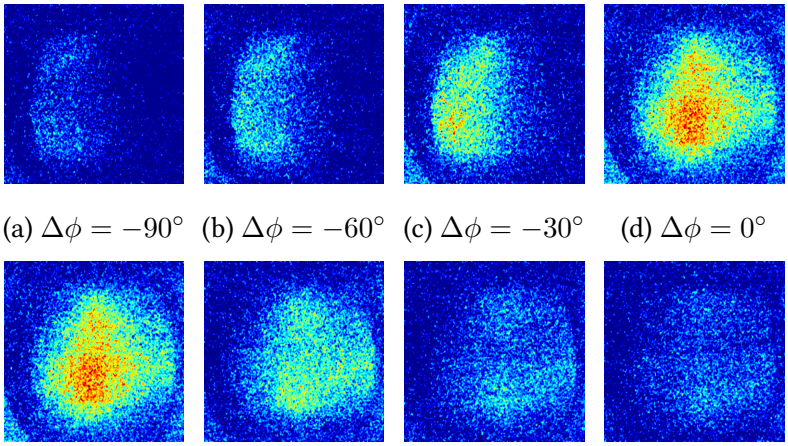

(a) $\Delta\phi = -90°$ (b) $\Delta\phi = -60°$ (c) $\Delta\phi = -30°$ (d) $\Delta\phi = 0°$

(e) $\Delta\phi = 0°$ (f) $\Delta\phi = 30°$ (g) $\Delta\phi = 60°$ (h) $\Delta\phi = 90°$

Figure 4.1: Measured atom beam image signals with different relative phases $\Delta\phi$ of the bichromatic frequencies. The inserted iris blocks ∼99% of the atom beam and leads to the low signal to noise ratio as compared to previous signals [16, 21]. The vacuum tube near the CCD camera can be seen at the edges of the images.

Figure 4.1 shows the signal of the atom beam imaging tool for different phases of the bichromatic frequencies. The clear dependence of the force on the relative phase difference of the light and even sign reversal is a key signature of the bichromatic force as mentioned in [22]. The low signal to noise ratio of the images is due to the inserted iris, which is blocking ∼99% of the atom beam so that only few metastable ^{40}Ar atoms reach the beam imaging chamber.

Although the atom beam imaging was a very useful tool to create the first signals of the bichromatic force, it was too unprecise to make quantitative measurements. The distance between the imaging tool and the bichromatic interaction zone was approximately two meters. For too large forces, the signal is cut off since the atoms collide with the wall of the vacuum chamber.

4.2 Observation of the Bichromatic Force

The first qualitative proof of the bichromatic force on metastable ^{40}Ar was performed with a fluorescence spectroscopy in the quench chamber. The atom flux monitoring [16]

was modified to detect the 811.754 nm fluorescence of the atoms which are excited with an additional laser beam. The laser could be tuned in the range of the velocity distribution and the fluorescence signal was strong enough to be detected by the modified optics.

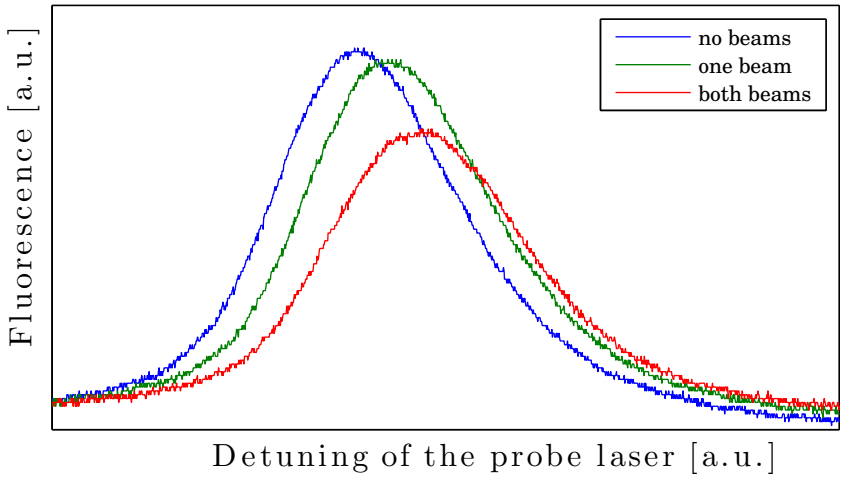

Figure 4.2: The signal of the fluorescence spectroscopy performed in the MOL chamber. Both beams together are stronger than one beam even though they are counter-propagating and deflect the atoms in different directions if used separately. This is a clear indication of the bichromatic force.

Figure 4.2 shows the detected fluorescence signal for a scan of the tuneable spectroscopy laser. The bichromatic beams are counter-propagating and deflect the atoms in different directions when they are turned on separately. However, both beams together show a dependence on the relative phase difference of the optical frequencies and exceed the deflection of one beam for certain phases. This is a clear indication for the bichromatic force.

The fluorescence spectroscopy is using existing optics that have been slightly modified. Unfortunately, the signal was very weak and increasing the power of the tuneable laser would lead to additional radiative forces. Therefore, all quantitative measurements that are presented in the next section have been done with absorption spectroscopy.

4.3 Characterization of the Bichromatic Force

The setup of the absorption spectroscopy is shown in Figure 3.6 of the last chapter. The frequency of the absorption laser is offset-locked [20] to the atomic resonance ω_A and can be tuned by several hundreds of MHz. This setup provides an absolute frequency scale to measure the velocity distribution of the atom beam.

The offset-lock can be used manually by setting different frequencies or by modulation with a function generator. The former method allows good frequency resolution and absolute values of the detunings while the latter is used for fast feedback of the signal with the loss of absolute frequency dependence. To combine the advantages of both methods, the absorption signal is measured once by manually locking the laser frequency at certain detunings. Assuming a constant velocity distribution of the atom beam, these acquired data points can be used to fit a frequency scale onto the modulated signals.

Figure 4.3 shows the absorption signal acquired with both methods. The manually taken data points are plotted as circles and have defined detunings. The scanned absorption signal is first fitted with a Voigt profile, since the absorption signal is a convolution of Gaussian Doppler profile and Lorentzian natural linewidth. This profile is then scaled to fit the manually acquired data points which gives an absolute frequency scale.

The width of the measured transverse velocity distribution is $[10.2 \pm 0.9]$ MHz which is significantly narrower than the distribution right after the source [11] due to the transverse collimator and the differential pumping stage, which acts as passive collimation. This leads to a good resolution of the Doppler shift that is added by the radiative or the bichromatic force.

The Doppler shift of a moving atom is given by (3.4). Using parameters of the Schaefter+Kirchhoff 60FC-4-A11-02 coupler with beam diameter of 1.97 mm, the theoretical maximal

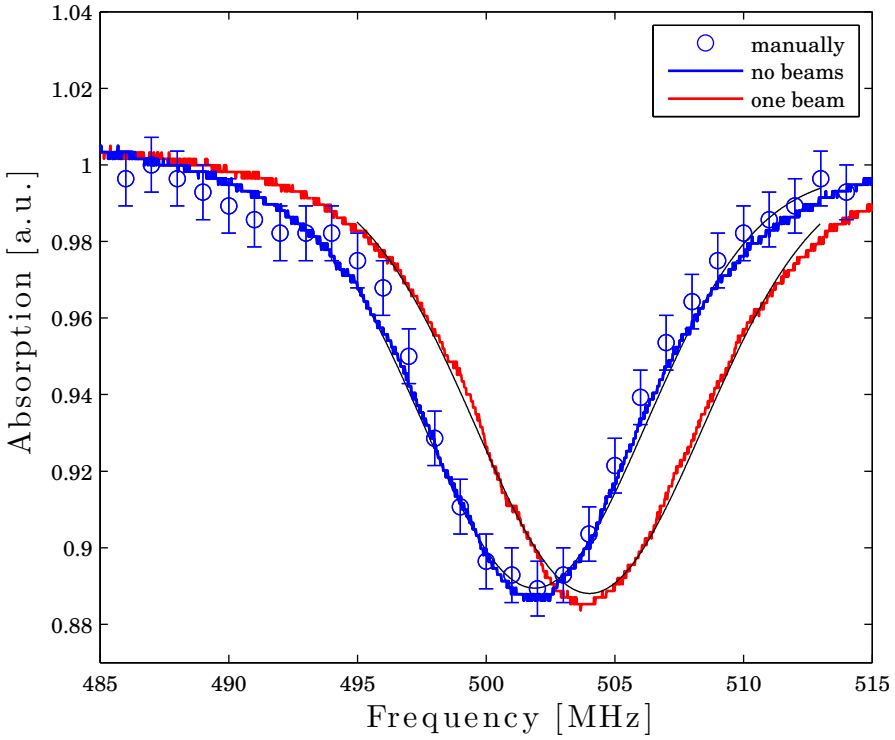

Figure 4.3: The manually acquired data of the absorption spectroscopy with defined detunings are shown as circles. The scanned absorption signals are fitted to these points to get an absolute frequency scale. The shifted absorption signal is taken with only one of the bichromatic beams on and is assumed to be deflected by the maximal radiative force. The solid curves are Voigt profiles fitted to the scanned signals.

Doppler shift with radiative force can be calculated and leads to:

$$\nu_{D,rad} = -k\frac{F_{rad,max}}{m}\frac{d}{v_{long}} = 2.26 \text{ MHz} \tag{4.1}$$

The dashed curve in 4.3 shows the absorption signal when only one of the bichromatic beams is used. The frequency difference using the distance of the minima is $[2.13 \pm 0.36]$ MHz and corresponds to the maximal radiative detuning within the error tolerances.

In the scope of this work, the bichromatic forces are measured in units of the maximal radiative force, which is obtained by blocking one of the beams. The intensity of the remaining bichromatic beam with center frequency ω_A is large enough, so that the maximal radiative force is achieved even though the beam is pulsed.

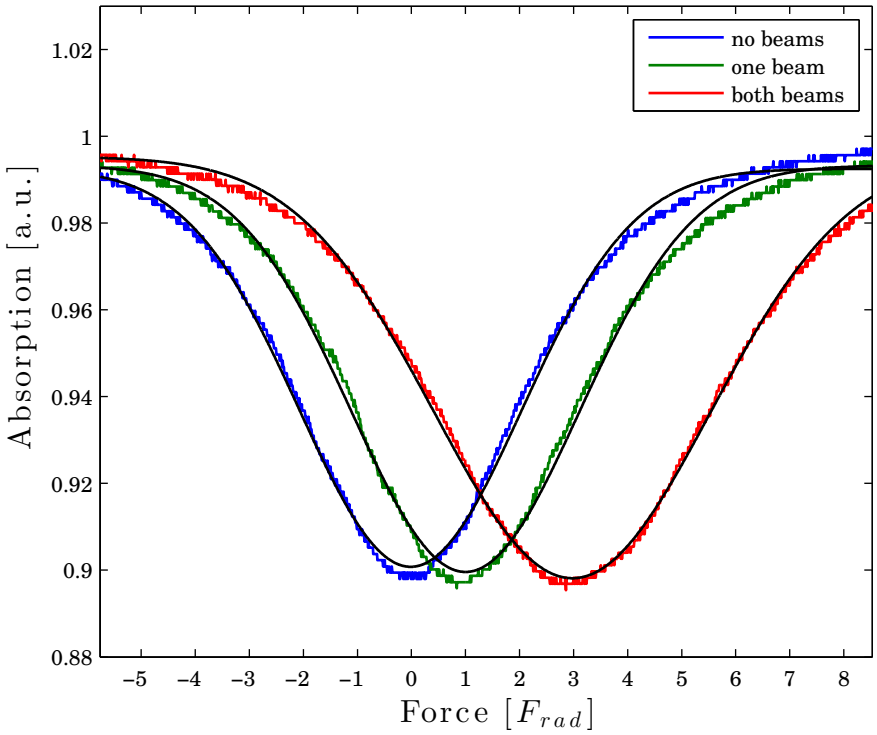

Figure 4.4: The absorption spectroscopy signal of the oscilloscope. The measured curves show the absorption with no laser beams, a single on-resonance frequency from one side and bichromatic beams with relative phase adjusted to the maximum Doppler shift of the signal. The absorption signal has a Voigt shape due to the convolution of Gaussian Doppler velocity distribution and Lorentzian natural linewidth [22]. The former is dominant, therefore the curves are fitted with a pure Gauss function.

The three curves in Figure 4.4 show the absorption signals with no deflecting laser beams, with one of the bichromatic beams turned on which acts with radiative force and with both bichromatic beams on, where the relative phase is adjusted to maximal detuning. The detuning is given in units of the maximal radiative detuning. The distance between the absorption minima gives the bichromatic force:

$$F_{BCF} = [2.95 \pm 0.54] F_{rad,max} \tag{4.2}$$

The error tolerance is the standard deviation of different measurements that have been performed with the same setup. In the scope of this work, the stability of the optical

setup and the resolution of the spectroscopy are the main contributions to the statistical error. The bichromatic force has been very sensitive to the alignment of the optical components which were therefore adjusted frequently. The resolution of the spectroscopy is good enough to separate the different signals, but will increase the statistical error since the width of the absorption is in the order of the expected detunings.

The measured bichromatic force in (4.2) is lower than the theoretically calculated force from the optical Bloch equations that is corrected for the Gaussian beam profile in Figure 2.14. This seems to be a systematic error in the setup, as all measured data are lower than expected. The possible reasons are discussed in the next chapter and a scaling factor of 0.8 is used on the theoretical curves in this section to have good agreement with the experimental data.

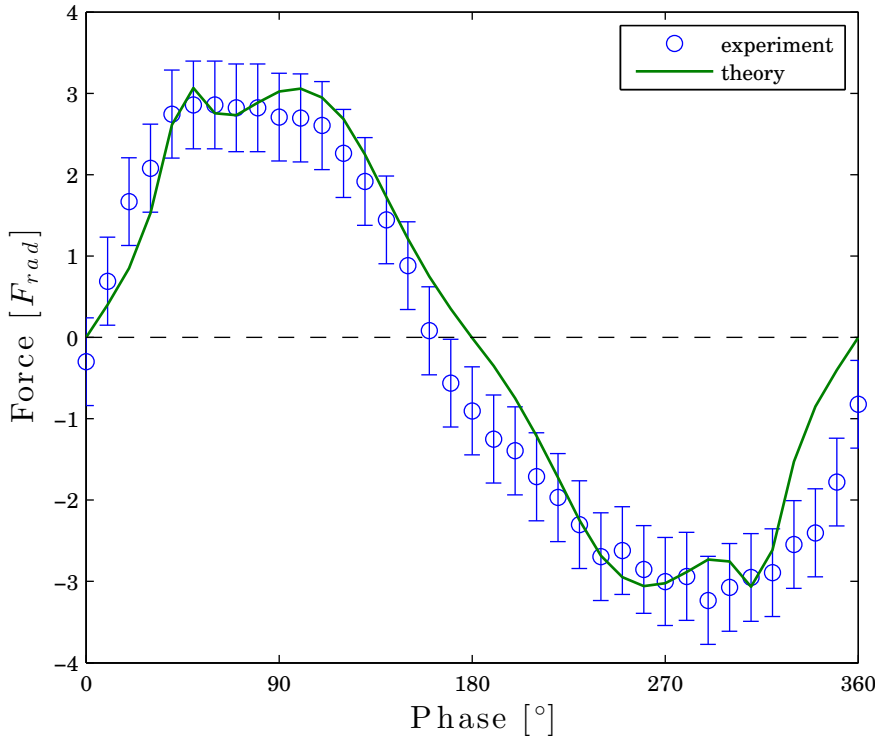

Figure 4.5: The bichromatic force measured with the absorption spectroscopy for different relative phases $\Delta\phi$ of the electric fields. The acoustic waves were changed by half the optical phase, since the light is passing twice through the AOM. As expected, the force changes sign with a phase change of $\Delta\phi = 180°$.

Figure 4.5 shows the bichromatic force in units of the maximal radiative force for differ-

ent relative phases of the frequencies. The force is zero for symmetric phase differences $\Delta\phi = 0°$ and $\Delta\phi = 180° = \pi$ and the absolute value is maximal for $\Delta\phi = \pm 90° = \pm\frac{\pi}{2}$. As expected, the force also changes direction, which is a key signature of the bichromatic force [22,26]. The theoretical phase curve is plotted as solid line and was calculated with the optical Bloch equations and corrected for the Gaussian beam profile. Here again, the theoretical values are scaled by 0.8. The correction for the Gaussian beam profile leads to a broader phase dependence of the force compared to the non-corrected theoretical phase curve in Figure 2.9.

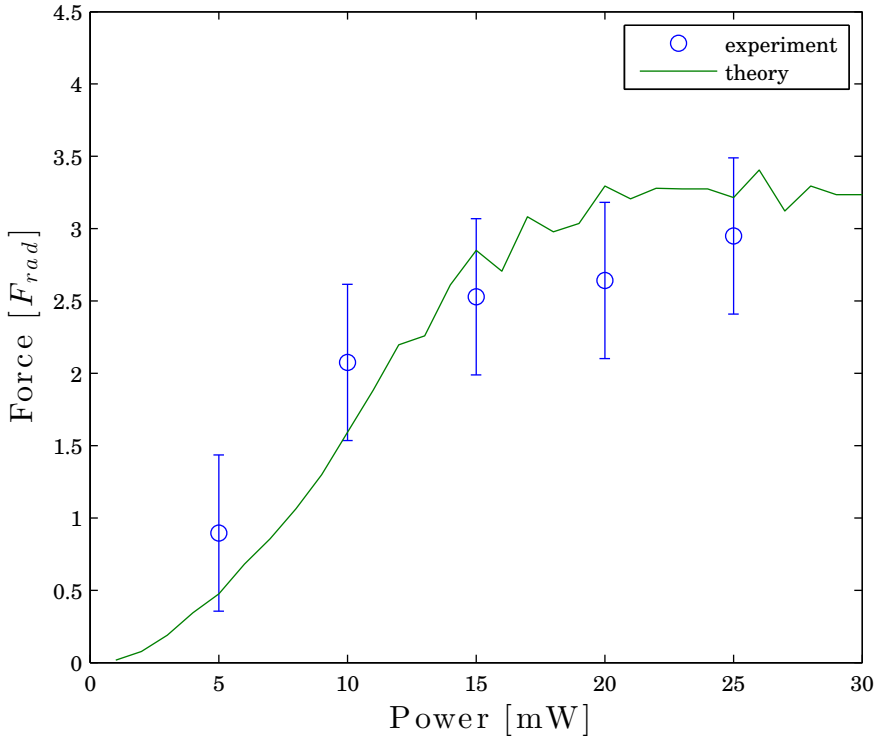

Figure 4.6: The bichromatic force with fixed detuning $\Delta = 65$ MHz measured for different powers of the laser beams. The solid line is the average of the calculated curves from 2.13. The highest power reached in the scope of this work is 25 mW per frequency, which leads to the largest bichromatic force.

The dependence of the bichromatic force with fixed detuning $\Delta = 65$ MHz on the optical power of the laser beams is shown in Figure 4.6. The measured data with a relative phase difference $\Delta\phi = 90°$ are plotted as circles and the mean of the theoretical curves calculated with the optical Bloch equations in Figure 2.13, scaled by 0.8, is shown as a solid line. The maximum force is achieved with a mean power of 50 mW, which gives

25 mW in per frequency. As expected from the theoretical curve, the force is saturated for larger power values and the highest achievable mean power of 50 mW is used for further measurements of the detuning Δ and the Doppler shifted force profiles.

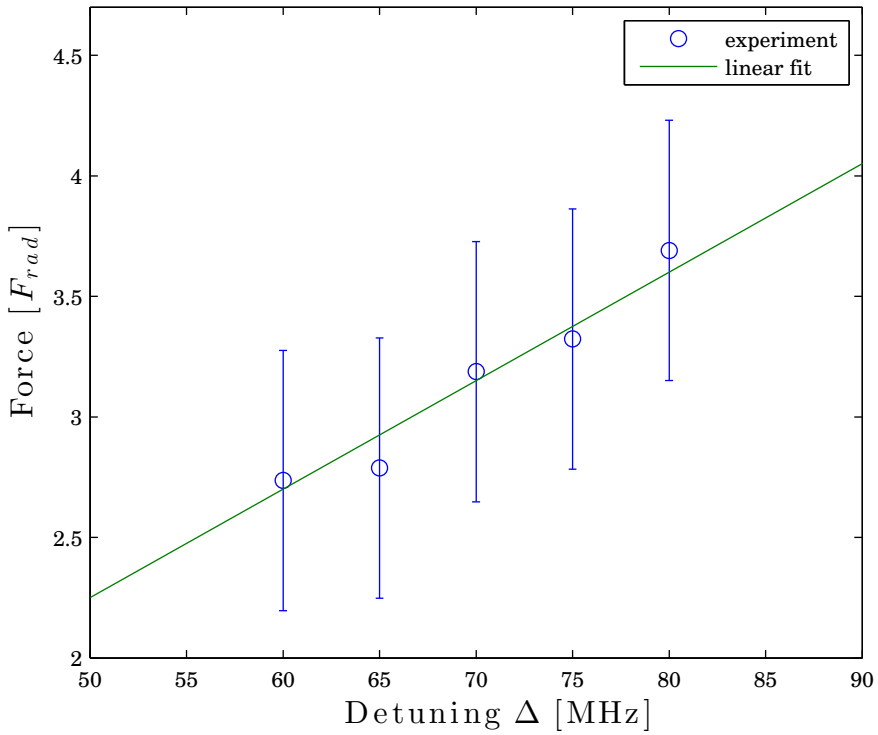

Figure 4.7: The bichromatic force for different detunings measured with mean power 50 mW, which gives 25 mW per frequency. The solid line is the scaled theoretical force given by (2.11) and the measured data points show the proportionality of the force with detuning Δ, as expected from the Doubly Dressed Atom model.

According to (2.11) of the Dressed State model, the bichromatic force is proportional to the detuning Δ of the light frequencies. Figure 4.7 shows measured data of the bichromatic force with different detunings Δ where the mean optical power of the beams is adjusted to 50 mW as described above. Since the performance of the AOM's were significantly lower for frequencies below 60 MHz and the upper limit of the Agilent 33250A frequency generator was 80 MHz, only this range could be covered. The solid line is a linear fit of the acquired data points and shows the proportionality of the force on the detuning frequency Δ.

The bichromatic force also depends on the Doppler shift ν_D of the atom, which shifts the atomic resonance ω_A from the center of the bichromatic frequencies in a laboratory reference frame. By adding $+kv_{trans}$ to the frequencies from one side and $-kv_{trans}$ to the frequencies from the other side, the same effect can be observed with a transversally collimated atom beam, since it will appear detuned in a reference frame moving with v_{trans}. This is used to measure the force profiles.

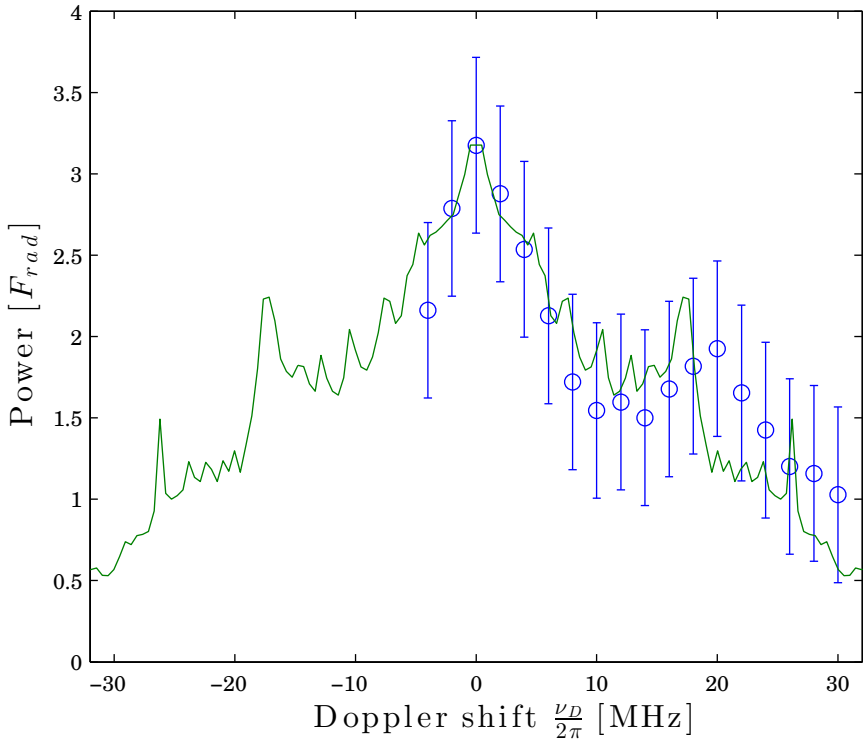

Figure 4.8: The measured bichromatic force profile for different detunings kv of the optical frequencies. The measured data points resemble the rough structure of the force profiles calculated with the optical Bloch equations and corrected with Gaussian beams, shown as the solid curve.

Figure 4.8 shows the measured data of the force for different Doppler shifts ν_D as circles. The theoretical values calculated from the optical Bloch equations and corrected with a Gaussian beam profile are plotted as solid curve. The acquired data points from the absorption spectroscopy show the expected large Doppleron resonance clearly, but although they resemble the rough structure of the theoretical curve, it seems they are shifted towards larger detunings. This can be explained by the simplicity of the model, that does not take additional recoil momentum of the photons and the longitudinal ve-

locity of the atoms into account. Even for small misalignments of the setup, the large longitudinal velocity $v_{long} \approx 274\frac{\mathrm{m}}{\mathrm{s}}$ [11] contributes to the Doppler shift.

The results of this chapter show a general good agreement of theory and experiment and the possibility to use the bichromatic force on metastable argon atoms. For practical uses, the strength of the force is only limited by the detuning Δ and therefore the available optical power to fulfill the intensity condition in (3.3). The theoretical values for constant Rabi frequencies over the cross section of the laser beams have to be corrected dramatically due to Gaussian beam profiles.

4.4 Bichromatic Precollimator

The intended task for the bichromatic force in ATTA was to cool down the transverse velocity of atoms leaving the metastable source into the capture range of the collimator [16, 19]. At the end of this work, an attempt for such a precollimator directly after the source was set up.

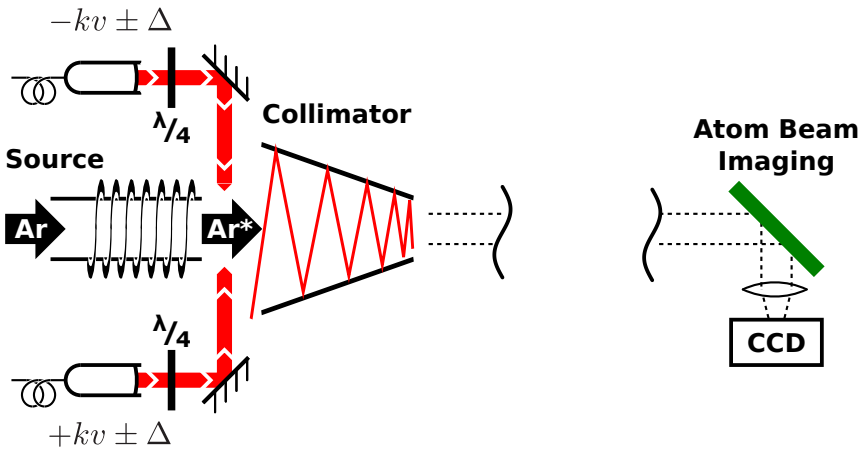

Figure 4.9: The setup for the attempt to precollimate the metastable argon atoms. More atoms are slowed down transversally to the capture range of the collimator [16,19] and the enhancement of the atom beam imaging signal can be measured.

Figure 4.9 shows the setup for the precollimation experiment performed in this work where the ^{40}Ar atoms can be pushed in one direction by the bichromatic force or in two

directions by the radiative force. The necessary Doppler shift ν_D was obtained by the maximal enhancement of the atom beam imaging signal. For $kv = 2\pi \cdot 25$ MHz, an enhancement of $\sim 7\%$ was observed for one radiative beam and $\sim 12\%$ for both beams. Here, the same Schaefter+Kirchhoff 60FC-4-A11-02 couplers with beam diameter of 1.97 mm are used as in the previous section.

However, the maximal enhancement using bichromatic beams with the same parameters as in the last section was only $\sim 3\%$ for a Doppler shift of $kv = 2\pi \cdot 35$ MHz and ideal phase $\Delta\phi = \frac{\pi}{2}$. The result is surprising since the measurements of the bichromatic force of the last section show that it exceeds the radiative force by a factor of ~ 3. This will be discussed in the next chapter.

Chapter 5

Conclusion

This chapter gives a brief summary of the work on the bichromatic force in the scope of the ATTA experiment. The conclusion with regard to the experimental results and an outlook for potential future improvements is presented in the following section.

5.1 Summary

The purpose of this work was to observe and characterize the bichromatic force on metastable ^{40}Ar, which has been demonstrated for other elements in previous works on that topic [12--15, 27, 32, 38]. The bichromatic force promises to exceed the radiative force if certain conditions can be fulfilled and has possible applications in the ATTA experiment for improving the ^{39}Ar detection efficiency.

Prior to this work, two tapered amplifiers have been set up to achieve the necessary optical power for the Rabi frequency condition in (3.3) and the amplification of the pulsed beams has been shown [36, 37]. The frequencies are generated by multi-mode double-pass AOM's shown in Section 3.1 and the adjustment of the relative phase difference of the optical beams by changing the phase of the sound waves of the AOM have be shown in Section 3.2. The amplified four-frequency light has been guided to the apparatus, where an interaction zone was set up in place of the MOL.

In the scope of this work, different detection methods have been tested. The atom beam

imaging tool was useful to observe the first bichromatic signal but was unsuited for quantitative measurements. A saturation spectroscopy on the $1s_5 \rightarrow 2p_9$ transition was performed as described in Section 3.3. The first attempt was in the quench chamber where the atom flux monitoring was modified to detect the 811.754 nm fluorescence, but the signal turned out very weak. An absorption spectroscopy directly after the bichromatic interaction region was set up to create stronger signals.

The resolution of the absorption spectroscopy was good enough to detect the Doppler shift of the atoms due to the radiative force. By blocking one of the bichromatic beams, the maximal radiative force could be measured and this was used as reference since the bichromatic force is given in units of the radiative force in this work.

The characteristics of the bichromatic force have been observed in different measurements as presented in Section 4.3. The experimental data cover the strength of the force, optimal light power, phase dependence of the force, dependence on the bichromatic detuning Δ and the dependence on the Doppler shift of the atoms. All measured bichromatic forces were lower than the theoretical predictions that include the Gaussian nature of the laser beams. A scaling factor of 0.8 due to systematic errors has been employed to fit the data.

5.2 Conclusion and Outlook

The bichromatic force on metastable ^{40}Ar atoms has been shown in this experimental work. The observed forces were clearly stronger than the radiative force and the strength and direction of the forces depend strongly on the relative phase difference of the optical frequencies. Both effects are key signatures of the bichromatic force and show its possible application to ^{40}Ar.

However, the measured bichromatic force is approximately half as strong as the expected forces from the basic calculations in Sections 2.1 - 2.3. An important correction of the

calculated force profiles considering Gaussian intensity distribution of the laser beams was introduced in Section 2.4. Including this, the Rabi frequency condition can not be fulfilled everywhere across a laser beam and the average force has to decrease in this case.

The experimental data are still slightly below the corrected theoretical calculated curves, which are therefore scaled by a factor of 0.8 to fit the data. There are several reasons for the remaining systematic errors that will be discussed in the following.

Overestimation of the interaction time for multi-level atoms: The description of the bichromatic force is using a two-level system in each of the presented models. Once the stretched states are reached, the magnetic sublevels m_J of ^{40}Ar can be neglected. However, it will take time to reach the stretched states and during this process, non-optimal conditions are given since the Rabi frequency is depending on the strength of the dipole transition. This effect leads to an overestimation of the effective interaction time and to verify this, the force could be measured with different interaction lengths. The mentioned effect should not increase in this case as it is independent of the beam diameter. An optical pumping to the stretched states beforehand should increase the force, but a quick attempt to do this in the scope of this work led to no effect and has to be investigated further in the future.

Frequency imbalances due to the tapered amplifier: The beating of the signals after the tapered amplifier was worse than the beating of the seeds, which had a visibility of $\nu_{vis} \approx 1$, that leads to imbalances of the four frequencies. This will decrease the bichromatic force, as all models presented in this work rely on the same power of each frequency. The advantage of overlapping the two frequencies before the amplification was to preserve laser power but due to non-linear effects, higher power of the TA could not be used. This should be taken into account and the laser beam should be amplified before passing the multi-mode AOM's in future setups on the bichromatic force.

Underestimation of the laser beam diameter for the radiative force: The interac-

tion length of the atoms with the radiative force is assumed to be the same as for the bichromatic force, but since a very high power is used, the cross section of the laser beam acting with radiative force will be larger than the width of the couplers. For measurements in future setups that use the presented method of this work, an iris should be used after the coupler to have a defined laser beam diameter.

Aside from the above-mentioned systematic errors, small misalignments can reduce the measured force. The bichromatic beams were adjusted with different tools but they may not have been perfectly perpendicular to the atomic beam and the overlap of the two beams may not have been perfect. Therefore, the introduced scaling factor of ~ 0.8 is used to correct potential systematic errors.

The measured bichromatic force in (4.2) is in agreement with the theoretical value within the error tolerance. The measurements show a clear signature of the bichromatic force on ^{40}Ar as it is larger than the radiative force and has a strong phase dependence. The signal of the atom beam imaging quantifies the atom flux in the MOT chamber. Its enhancement using a bichromatic precollimator was lower than the signal with the same setup using the radiative force. This is surprising as the measured bichromatic force exceeds the radiative force by a factor of ~ 3. Since the interaction region was directly after the source tube, this could be an effect of the RF-discharge in the metastable argon source as the magnetic field is changing with ~ 130 MHz. This has to be investigated in future works before setting up a bichromatic precollimator. If the RF-discharge is the problem, optical excitation or DC-discharge sources could overcome this.

Even if the above-mentioned problem can be solved, previous bichromatic collimation experiments still required four times the interaction length of a radiative collimation since each direction has been set up independently. Therefore, the parameters in this work are not sufficient to surpass a radiative precollimator as the bichromatic force was only [2.95 $\pm$0.54] times stronger than the radiative force. According to the linear dependency of the bichromatic force on the detuning Δ in Figure 4.7, a minimum detuning of $\Delta = 2\pi \cdot 90$ MHz is required to be more efficient than in the radiative case. This requires

a mean power of ~ 100 mW that could not be achieved with the current setup due to non-linear effects of the tapered amplifier. Therefore, a radiative precollimator will be included in the current setup, where an enhancement of $\sim 12\%$ in one dimension has been measured for non-optimal beam diameters of 2 mm.

However, under certain conditions, it should be possible to overlap two pairs of bichromatic beams which would halven the interaction length. In the same dimension (e.g. horizontal or vertical), the three frequencies ω_A and $\omega_A \pm 2\Delta$ lead to a bichromatic force from both directions with center at $\nu_D = \pm kv = \pm\Delta$. It is also possible to overlap the interaction region of perpendicular beams by adjusting the relative phase difference of each frequency to $\Delta\phi = \frac{\pi}{2}$, which requires four synchonized frequencies.

This work presented a first study of the bichromatic force on Argon and many parameters are chosen for experimental convenience. It turned out that the subject was more complex than in the simple π-pulse model that has been used for a first attempt at the beginning of this work. The more advanced Doubly Dressed Atom model and numerical calculations have been studied afterwards and the presented experimental data could be explained with these theoretical considerations. From the author's point of view, the presented results were satisfying for the characterization of the bichromatic force.

Appendix A

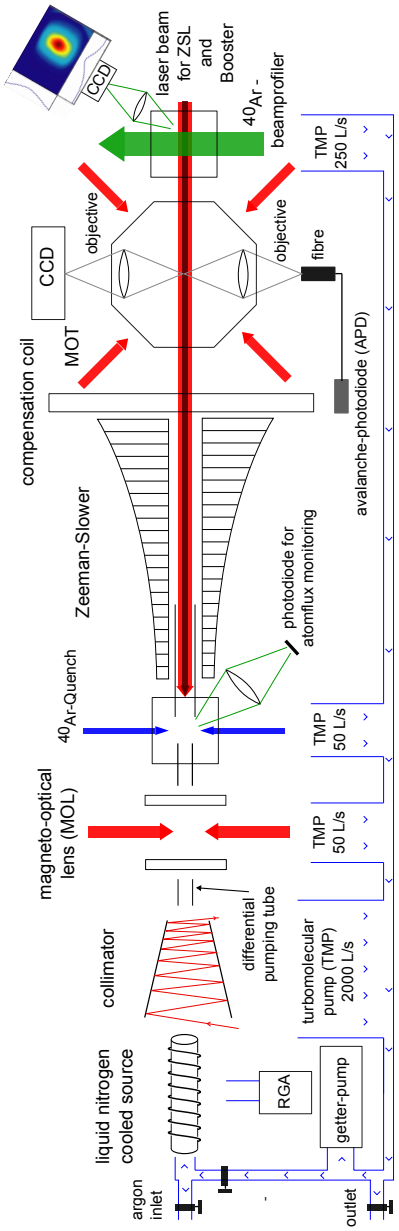

Figure 5.1: A detailed schematic diagram of the ATTA apparatus in 2013 [16].

Appendix B

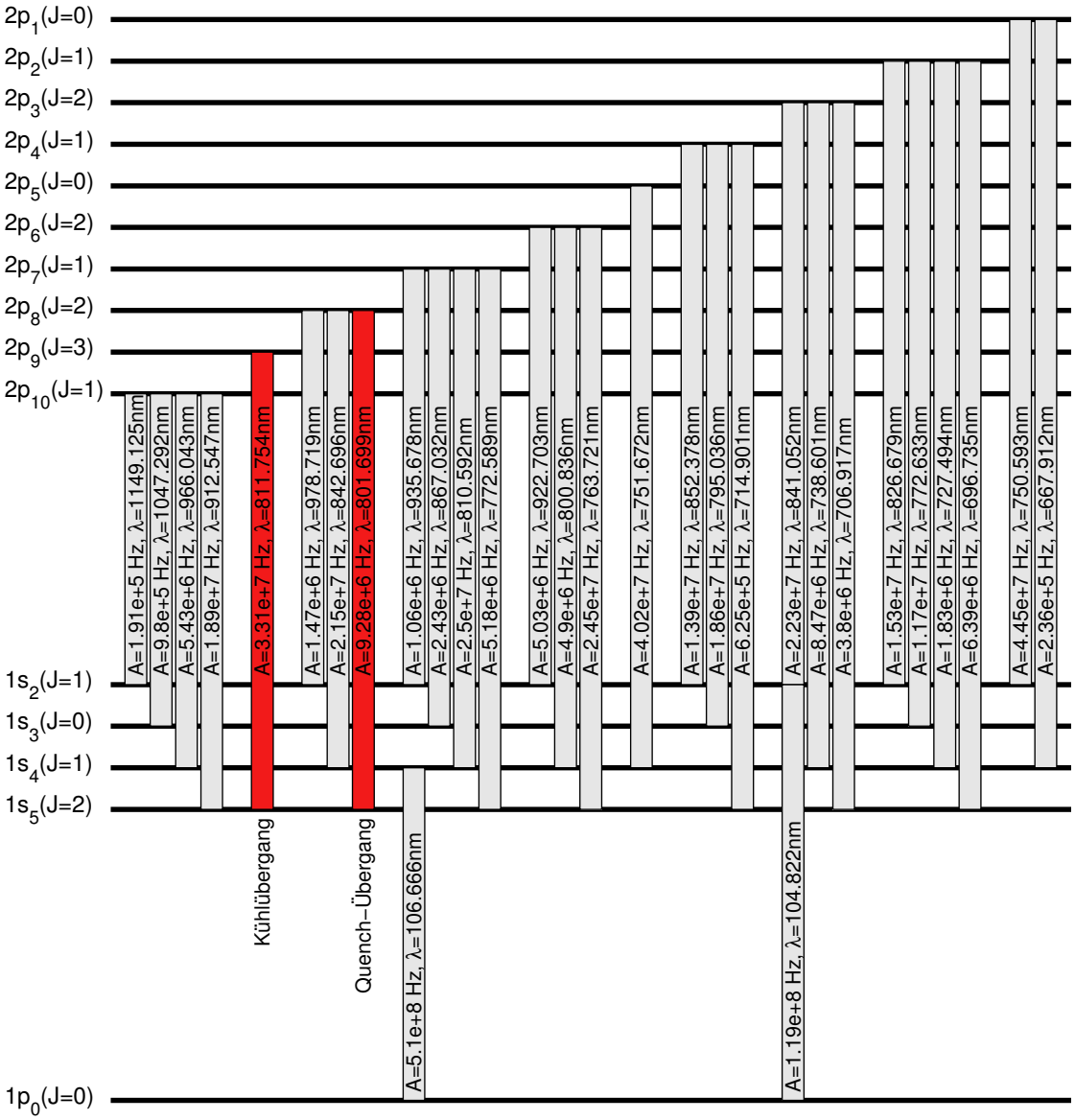

Figure 5.2: A detailed schematic diagram of the ^{40}Ar transitions [21].

Appendix C

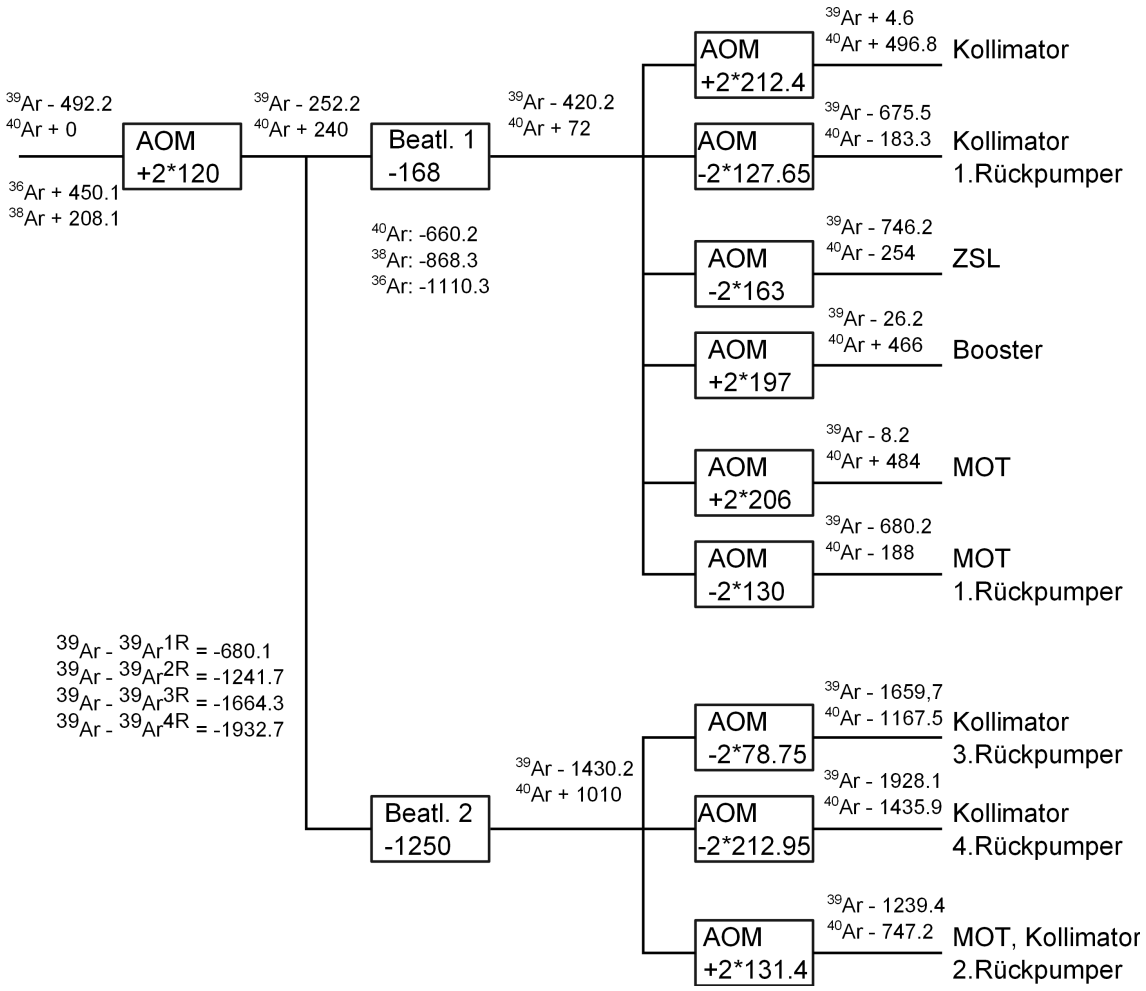

Figure 5.3: A schematic diagram of the laser system [21].

Appendix D

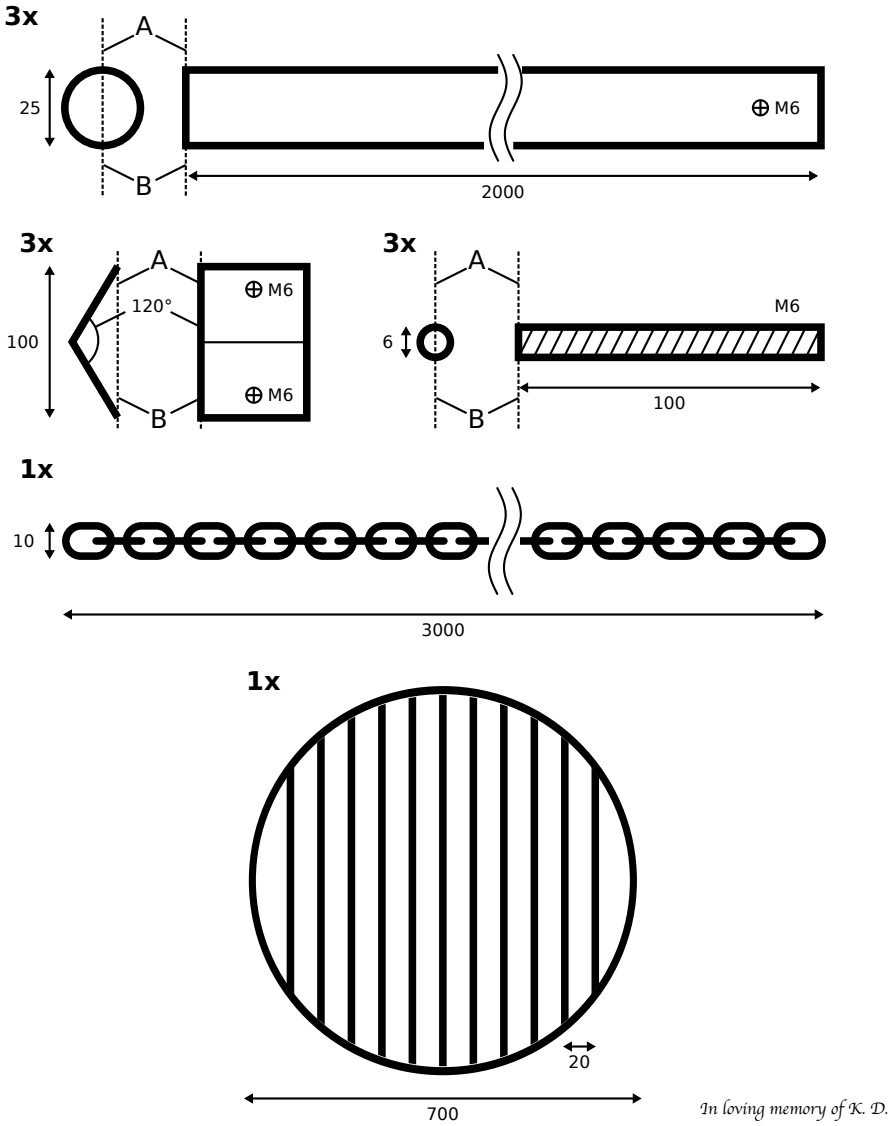

Figure 5.4: A schematic diagram of the Schwenkersystem used in the scope of this work. Only the components of the Schwenker are shown here where the Schwenker and the Schwenker are not included for simplicity.

Bibliography

[1] H.H. Loosli, B.E. Lehmann, and W.M. Jr. Smethie. Noble gas radioisotopes: ^{37}Ar, ^{85}Kr, ^{39}Ar, ^{81}Kr. *Environmental Tracers in Subsurface Hydrology*, pages 379--396, 2000.

[2] O. A. Schaeffer R. W. Stoenner and S. Katcoff. Half-lives of ^{37}Ar, ^{39}Ar, and ^{42}Ar. *Science*, 148:1325--1328, 1965.

[3] H.H. Loosli and H. Oeschger. ^{39}Ar, ^{14}C and ^{85}Kr measurements in groundwater samples. *IAEA Vienna: Isotope Hydrology*, 2:931, 1978.

[4] P. Collon, W. Kutschera, and Z.-T. Lu. Tracing noble gas radionuclides in the environment. *Annual Review of Nuclear and Particle Science*, 54(1):39--67, 2004.

[5] J. Welte. *Atom Trap Trace Analysis of ^{39}Ar*. PhD thesis, Faculty of Physics and Astronomy, University of Heidelberg, www.matterwave.de, 2011.

[6] IAEA. Environmental isotopes in the hydrological cycle. *Water resources Programme*, 1, 2000.

[7] C. Y. Chen, Y. M. Li, K. Bailey, T. P. O'Connor, L. Young, and Z.-T. Lu. Ultrasensitive Isotope Trace Analyses with a Magneto-Optical Trap. *Science*, 286(5442):1139--1141, 1999.

[8] W. D. Phillips, J. V. Prodan, and H. J. Metcalf. Laser cooling and electromagnetic trapping of neutral atoms. *JOSA B*, 2(11):1751--1767, 1985.

[9] J. Welte, F. Ritterbusch, I. Steinke, M. Henrich, W. Aeschbach-Hertig, and M. K. Oberthaler. Toward the realization of atom trap trace analysis for ^{39}Ar. *New Journal of Physics*, 2010.

[10] F. Ritterbusch, S. Ebser, J. Welte, T. Reichel, A. Kersting, R. Purtschert, W. Aeschbach-Hertig, and M. K. Oberthaler. Groundwater dating with Atom Trap Trace Analysis of ^{39}Ar. *Geophysical Research Letters*, 41(19):6758--6764, October 2014.

[11] Z. Feng. Implementierung einer Atomflussüberwachung für ^{39}Ar ATTA, 2012.

[12] V. Voitsekhovich, M. Danileiko, A. Negriiko, V. Romanenko, and L. Yatsenko. Optical pressure on atoms in a field of counterpropagating amplitude- and frequency-modulated waves which are in resonance with an atomic transition. *Soviet Journal of Quantum Electronics*, 21(9):996--998, 1991.

[13] J. Söding, R. Grimm, Yu. B. Ovchinnikov, Ph. Bouyer, and Ch. Salomon. Short-Distance Atomic Beam Deceleration with a Stimulated Light Force. *Phys. Rev. Lett.*, 78(8):1420--1423, 1997.

[14] M. R. Williams, F. Chi, M. T. Cashen, and H. Metcalf. Measurement of the bichromatic optical force on Rb atoms. *Phys. Rev. A*, 60(3):1763--1766, 1999.

[15] M. T. Cashen and H. Metcalf. Bichromatic force on helium. *Phys. Rev. A*, 63, 2001.

[16] F. Ritterbusch. *Dating of groundwater with Atom Trap Trace Analysis of ^{39}Ar.* PhD thesis, Faculty of Physics and Astronomy, University of Heidelberg, 2013.

[17] J. Welte. Single Atom Detection By Fluorescence. Master's thesis, Faculty of Physics and Astronomy, University of Heidelberg, 2007.

[18] C. Kaup. Single-Atom Detection of ^{39}Ar. Master's thesis, Faculty of Physics and Astronomy, University of Heidelberg, 2011.

[19] F. Ritterbusch. Realization of a collimated beam of metastable atoms for ATTA of ^{39}Ar. Master's thesis, Faculty of Physics and Astronomy, University of Heidelberg, 2009.

[20] M. Henrich. Design and Realization of a Laser System for ATTA of ^{39}Ar. Master's thesis, Faculty of Physics and Astronomy, University of Heidelberg, 2010.

[21] Sven Ebser. Optimierung und Stabilisierung von ^{39}Ar-ATTA bis hin zur erstmaligen Anwendung auf die Datierung natürlicher Wasserproben. Master's thesis, University of Heidelberg, 2012.

[22] H. J. Metcalf and P. van der Straten. *Laser cooling and trapping*. Springer, New York ; Berlin ; Heidelberg [u.a.], 1999.

[23] J. J. Sakurai and S. F. Tuan. *Modern quantum mechanics*. Addison-Wesley, 1985.

[24] B. H. Bransden and C. J. Joachain. *Physics of Atoms and Molecules*. Longman, 1983.

[25] Claude Cohen-Tannoudji, Jacques Dupont-Roc, and Gilbert Grynberg. *Atom-photon interactions*. Wiley-VCH, Weinheim, 2004.

[26] H. J. Metcalf and P. van der Straten. Laser cooling and trapping of atoms. *J. Opt. Soc. Am. B*, 20(5):887--908, 2003.

[27] M. J. Partlow. *Bichromatic Collimation to Make an Intense Helium Beam*. PhD thesis, Stony Brook University, 2004.

[28] L. Allen and J. Eberly. *Optical resonance and two-level atoms*. Wiley, 1975.

[29] R. Grimm, J. Soeding, Y. B. Ovchinnikov, and A. I. Sidorov. Sub-Doppler manifestation of the magneto-optical radiation force. *Opt. Commun.*, 98(1):54--60, 1993.

[30] L. Yatsenko and H. Metcalf. Dressed-atom description of the bichromatic force. *Phys. Rev. A*, 70:063402, Dec 2004.

[31] L. Landau and E. Lifshitz. *Quantum mechanics*. Pergamon, 1958.

[32] M. C. Keller. Optical Manipulation of Helium Atoms with Application to Neutral Atom Lithography. Master's thesis, Stony Brook University, 2006.

[33] http://mathworks.com/help/matlab/ref/ode23.html.

[34] J. J. Tollett, J. Chen, J. G. Story, N. W. M. Ritchie, C. C. Bradley, and Randall G. Hulet. Observation of velocity-tuned multiphoton "Doppleron" resonances in laser-cooled atoms. *Phys. Rev. Lett.*, 65(559), 1990.

[35] B. E. Saleh and M. C. Teich. *Fundamentals of photonics*. Wiley, Hoboken, N.J., 2007.

[36] A. Mil. Realization of an amplified optical beating for bichromatic cooling of metastable argon, 2013.

[37] M. Pruefer. Aufbau eines temperaturstabilisierten optischen Verstaerkers. Technical report, Faculty of Physics and Astronomy, University of Heidelberg, 2013.

[38] M. A. Chieda and E. E. Eyler. Bichromatic Slowing of Metastable Helium. *Phys. Rev. A*, 86(5), 2012.

Acknowledgement

Ich möchte besonders meinem Betreuer **Prof. Dr. Markus K. Oberthaler** dafür danken, dass er mir diese Masterarbeit ermöglicht hat und mich bereits seit meiner Bachelorarbeit hilfreich in allen physikalischen und sonstigen Angelegenheiten unterstützt.

Prof. Dr. Matthias Weidemüller danke ich für die Zweitkorrektur dieser Arbeit und für die motivierenden Vorlesungen in den ersten beiden Semestern meines Studiums.

Sven Ebser und **Florian Ritterbusch** danke ich für die wunderbare Aufnahme in das ATTA Team, die Diskussionen rund um das Experiment und das Zeigen des vielseitigen Repertoire der Labortricks.

Ich möchte **Alexander Mil** und **Maximilian Prüfer** für ihre Vorarbeiten danken.

Ich danke **Anke Heilmann**, **Anika Frölian** und **Maurus Hans** für die Hilfe, die schöne Zeit und die netten Gespräche im Büro und Labor.

Bei meiner Freundin **Angelika Klein** möchte ich mich für Korrekturlesen der Arbeit bedanken. Sie war immer an meiner Seite in guten wie auch in schlechten Zeiten.

Christiane Vinck danke ich für ihre Korrekturen zur englischen Sprache, die mir noch weniger vertraut ist als die deutsche.

Meiner Familie **Yuanhua Feng**, **Suju Ge** und **Katharina Feng** danke ich herzlich für alles was sie für mich getan haben.

Magdalena und Axel Klein danke ich für ihre Unterstützung während des Studiums.

Ich möchte des Weiteren folgenden Personen danken…

…**Tobias Rentrop** für die aufregenden Mountainbike Exkursionen.

…**Arno Trautmann** für die Zurückhaltung bei meinen LaTeX-Defiziten.

…**Helmut Strobel** für diverse coole physikalische Experimente am Abend.

…**Wolfgang Müssel** für das ordentliche Verwalten der Liste der Schande.

…**Daniel Linnemann** für seine Recherchen am Reispaper.

…**Philipp Kunkel** für sein Entlasten der Frühstückskasse durch Eigenkreationen.

…**Philippe Bräunig** für das freiwillige Ausleihen diverser Geräte.

…und allen anderen **Matterwavern** und **KIPianern** für die Unterstützung und Unterhaltung währnd meiner Zeit am Institut.

Ich möchte mich auch bei **Maria Engel**, **Anouk Ehreiser**, **Anna Penzlin**, **Alexander Broska** und **Stefan Dorsch** für die schönen ersten Semester des Physikstudiums bedanken.

Erklärung:

Ich versichere, dass ich diese Arbeit selbstständig verfasst habe und keine anderen als die angegebenen Quellen und Hilfsmittel benutzt habe.

Heidelberg, den (Datum) .....